

Contents lists available at [ScienceDirect](https://www.sciencedirect.com)

Comput. Methods Appl. Mech. Engrg.

journal homepage: www.elsevier.com/locate/cma

A localized subdomain smoothing MMALE particle method for efficient modeling FSI problems[☆]

Zixian Sun, Ruichen Ni, Zhixin Zeng, Xiong Zhang^{*}

School of Aerospace Engineering, Tsinghua University, Beijing 100084, PR China

ARTICLE INFO

Keywords:

Multi-material arbitrary Lagrangian Eulerian method
 Particle method
 Localized mesh smoothing method
 Fluid–structure interaction
 Efficient runtime treatment

ABSTRACT

Fluid–structure-interaction (FSI) phenomena with multi-phase flow dynamics and structural damage commonly exist in engineering practice, which however bring great challenges to nowadays numerical FSI algorithms. A novel localized subdomain smoothing MMALE particle method (ls-ALEPM) is proposed in this paper for efficient and accurate simulations of large scale FSI problems. The MMALE method and the MPM are strongly coupled by immersing the MPM particles into the MMALE grid. In order to avoid the spurious strain induced by the mixed FSI velocity field, a decoupled stress updating scheme is proposed to update the stress of solid particles by introducing a virtual velocity field in the vicinity of FSI interface. And specifically, the highly accurate polyhedron intersection based method is employed for its remapping phase, which however is time-consuming. Thus, the localized subdomain smoothing method (LSSM) is put forward to accelerate the remapping phase which only involves the distorted regions of computational grid. The LSSM is composed of a distorted subdomain determination step and a combined mesh smoothing step. Each iteration of the combined mesh smoothing step consists of the modified GETMe and the weighted average method, and the transfinite interpolation method is adopted if the quality criteria is still not satisfied after prescribed maximum number of iterations. The validity and efficiency of ls-ALEPM is verified by several benchmark numerical examples and practical engineering simulations.

1. Introduction

Fluid–structure-interaction (FSI) phenomena with multi-phase flow dynamics commonly exist in porous media [1–4], structural damage due to blast loading [5–7], nuclear [8,9] and water entry of structures [10–13]. It is of great significance to figure out the corresponding mechanism for physical applications. However in extreme events, these complicated FSI problems always involve multi-phase flow dynamics, shock discontinuity and even structural topology change with dynamic failure, and bring great challenges to both theoretical and experimental research. Therefore, it is worth developing efficient and accurate numerical algorithms to simulate these phenomena.

Plenty of numerical methods aiming at accurate simulations of the multi-phase fluid flow have been put forward in these decades. According to the kinematic description, traditional methods can be classified into two categories as Eulerian methods and Lagrangian methods. In Eulerian methods, the computational grid is fixed in space and can handle multi-phase flow dynamics with large distortion easily. However the detection of complicated multi-phase interface motion is still a challenge. In Lagrangian methods, the computational grid is embedded and deformed with the material which is natural for the sharp multi-phase interface to be captured and maintained [14]. Traditional Lagrangian methods will encounter numerical difficulty of heavily distorted mesh in

[☆] Supported by the National Natural Science Foundation of China (12172192).

^{*} Corresponding author.

E-mail address: xzhang@tsinghua.edu.cn (X. Zhang).

<https://doi.org/10.1016/j.cma.2023.116676>

Received 18 August 2023; Received in revised form 9 November 2023; Accepted 29 November 2023

0045-7825/© 2023 Elsevier B.V. All rights reserved.

simulating fluid problems with large deformation. Arbitrary Lagrangian-Eulerian (ALE) methods [15–17] are raised by combining the advantages of both Eulerian method and Lagrangian method. Indirect ALE methods [6,18,19] with operator splitting are widely used and consist of Lagrangian phase, rezoning phase and remapping phase. By solving governing equations in the Lagrangian form, ALE methods maintain the precise material interface description in the Lagrangian phase. Then a new grid with better quality is obtained in the rezoning phase to deal with mesh distortion. In traditional ALE methods, every single cell possess only one kind of materials, so that the rezoned grid should snap to the multi-phase interface for accuracy [20]. The Multi-Material Arbitrary Lagrangian-Eulerian (MMALE) presented by Peery et al. [21] allows multiple materials to exist in a single cell and still deals with the complex material interface very well with the help of MOF method[22,23]. MOF method stores both the material centroid and volume fraction in each cell and is proved to be the most accurate multi-phase interface construction method[24,25]. Qing et al. [24,26] presented a robust MoF method for severely deformed polygonal mesh and developed a discontinuous Galerkin CCALE-MOF method in axisymmetric geometry. Finally, the physical variables are transferred from the old grid to the newly created one in the remapping phase. Several kinds of remapping methods have been presented before. Flux based methods and swept-region based methods [27–30] suffer from the restricted displacement between the new grid and old one. Moreover, flux based methods use fluxes through surfaces of neighboring cells and thus require the same connectivity of the grids. The intersection based methods [31,32] conduct accurate multi-phase remapping process through exact subdivisions and intersections, which has no restriction in connectivity and proximity of grids. However intersection based methods are time-consuming which even account for more than 90% of the total simulation time in large-scale engineering problems.

Many attempts have been made to enhance the efficiency of remapping phase in MMALE. Chen et al. [33] improved the 3D polyhedron intersection based method [34] with “clipping and projecting” algorithm, which enhances the efficiency and robustness of remapping phase. Bernadt et al. [35] presented a hybrid remapping method in which subdomains occupied by single material are remapped by computationally cheap swept-region remapping while multi-material cells are remapped by intersection-based remapping. Yang et al. [36] developed a new flux-based hybrid subcell-remapping method which realized direct remapping of the subcell masses. Although the swept-region remapping requires the rezoned grid to be close to the old grid, hybrid remapping is efficient and innovative as it narrows the region of intersection-based remapping while retaining the accuracy. In fact, narrowing the intersection area can also be realized by changing the rezoning phase. Since mesh distortion mainly occurs in the vicinity of FSI interface [37] or other localized regions in most of FSI problems, global remapping with re-division of the whole computational grid is time-consuming and unnecessary while localized rezoning combined with mesh improving methods is more appropriate to realize efficient remapping treatment.

Mesh improving methods have been well documented in the past years [21,38,39]. Among them, methods with topology altering are very effective in dealing with unstructured meshes [40] but suffer from complex operations and freshly generated cells of low quality. Mesh smoothing methods which improve the mesh only by relocation of nodes without changing topological relationship are robust and more appropriate for structured grids. These methods can be classified as optimization based methods [41,42], physical analogy methods [38,43,44], Laplacian method and its variants [45,46], geometric element transformation methods [47–50]. Optimization based methods determine the objective function according to quality of grid and improve the grid through optimization algorithms, which have good versatility but suffer from high computational complexity and cost. Physical analogy methods are considered to be the most effective mesh improving methods and adopt a fictitious elastic problem [38,51] solved on the mesh domain. However it also suffers from the high computational cost which is caused by assembly and solution of large-scale matrix. Meduri [51] presented a faster algorithm by smoothing only a single layer of neighbor tetrahedral elements of distorted ones, which is a good innovation for introducing local mesh regions but the smoothing region is limited quite small. The Laplacian method [52,53] which moves nodes to the arithmetic average of their adjacent nodes is the most commonly used method but it may cause illegal or even invalid cells [54]. Kim et al. [55] developed a two-step Laplacian mesh smoothing technique to improve the quality of trimmed hexahedral cells while preserving the sharp features. Di et al. [45] and Aymone et al. [56] adopted the weighted average method which is similar to Laplacian method and achieved computationally cheap and effective mesh smoothing. The geometric element transformation methods which transform single elements and determine new node positions by averaging nodes have attracted wide attention. Vartziotis et al. [50] presented a dual element based GETMe for all-hexahedral mesh smoothing whose results are comparable to global optimization-based approach while being faster. Meduri et al. [51] developed a smoothing method which combined an elastic analogy method with GETMe to overcome few critical situations where elastic analogy method is less effective, showing that combining different methods into a whole can take full advantages of different methods and obtain more effective methods by complementarity.

Recent literature has proposed or promoted several methods to simulate the interaction of multi-phase fluids and structures with large deformations. Zhang et al. [57,58] established a novel theory for the bubble dynamics which unifies different classical bubble equations successfully and proposed a multi-phase SPH method to simulate the flooding of a damaged cabin. Ni et al. [59] proposed a novel immersed boundary method based on Lagrangian multiplier and successfully applied it to the analysis of structures under blast load. Zheng et al. [60] coupled the phase-field lattice Boltzmann and material point method for FSI problems involving large density and viscosity contrasts. Xiao et al. [61] developed a non-intrusive reduced order model for FSI problems based on proper orthogonal decomposition and radial basis function interpolation method. Chen et al. [62] coupled the Weakly Compressive SPH with FEM for hydroelastic problems and Xue et al. [63] proposed a coupled Riemann SPH–RKPM to simulate weakly compressible fluid–structure interaction problems. Mostafaiyan et al. [64] adopted MLS-FEM to predict pressure discontinuities of multi-phase flow fields. Kan and Zhang coupled staggered MMALE and MPM based on the concept of the immersed boundary method [65,66] and presented an MMALE particle method [67]. The MMALE particle method immerses the MPM particles into MMALE cells and tracks the interfaces between the fluid and structure implicitly. By assembling the nodal force and the nodal momentum from both the solid particles

and fluid cells, the interface interactions are implicitly implemented and a no-slip boundary condition is maintained naturally. The MMALE particle method benefits from both the advantages of the material point method (MPM) widely used in extreme events and MMALE with significant advantages mentioned before, and is proved to be an effective method. However it suffers from spurious strain in structures because of the mixed velocity field adopted at the FSI interface. As the solid structures and fluids have significant differences in compressibility, updating the strain and stress of solid particles near the FSI interface with the mixed nodal velocities is unreasonable and thus a new updating scheme of the MMALE particle method is required.

In the present work, a novel localized subdomain smoothing MMALE particle method (ls-ALEPM) is proposed for efficient and accurate simulations of large scale FSI problems. The MMALE method and the MPM are strongly coupled by immersing the MPM particles into the MMALE grid. In order to avoid the spurious strain induced by the mixed FSI velocity field, a decoupled stress updating scheme is proposed to update the stress of solid particles by introducing a virtual velocity field in the vicinity of FSI interface. And specifically, the highly accurate polyhedron intersection method is employed for the remapping phase, which however is time-consuming. Thus, a localized subdomain smoothing method (LSSM) is put forward to accelerate the remapping phase which only involves the distorted regions of computational grid. The LSSM is composed of a distorted subdomain determination step and a combined mesh smoothing step. The combined mesh smoothing step adopts the GETMe for rapidly preconditioned mesh smoothing and the weighted average method for further delicate process in each iteration step. And the transfinite interpolation method is adopted if the quality criteria is still not satisfied after prescribed maximum number of iterations. Several numerical examples, including smoothing benchmark of 3D distorted grid, Sedov point explosion problem, moving projectiles in fluid, fragmentation of a cylinder shell induced by blast and structural damage of open-frame building under explosion, are studied to verify and validate the proposed ls-ALEPM, and numerical results are in good agreement with experiments and show its efficiency and robustness.

The paper is structured as follows. Governing equations of the MMALE particle method are briefly introduced in Section 2. Then a decoupled stress updating scheme is presented for the Lagrangian phase in Section 4, and a localized subdomain smoothing method for Euler phase is presented in Section 5. Flowchart of the localized subdomain smoothing MMALE particle method is described in Section 6. Validations and benchmark simulations are presented in Section 7. Finally, conclusions are drawn in Section 8.

2. Governing equations

The governing equations of continuum mechanics in the updated Lagrangian frame are

$$\begin{aligned}\dot{\rho} &= -\rho \dot{u}_{i,i} \\ \rho \ddot{u}_i &= \sigma_{ji,j} + \rho b_i \\ \rho \dot{e} &= \dot{\epsilon}_{ij} \sigma_{ij}\end{aligned}\quad (1)$$

where the overdot denotes derivative with respect to time, ρ is the current density, e is the specific internal energy, the subscripts i and j indicate the components of the spatial variables following the Einstein convention, u_i is the displacement, b_i is the body force per unit mass, σ_{ij} is the Cauchy stress, ϵ_{ij} is the Cauchy strain. Note that the comma in the subscript denotes the derivative.

With the concept of the immersed boundary method [66], the solid structures are immersed in the fluid domain and the FSI interface is implicitly tracked by the location of solid as shown in Fig. 1.

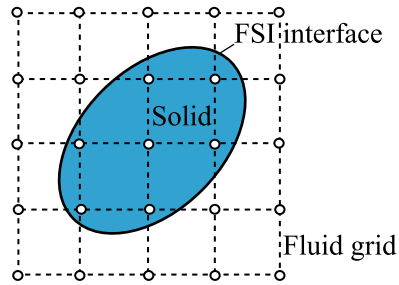


Fig. 1. FSI with the immersed boundary method.

Thus, the density, stress and internal energy can be expressed as

$$\begin{aligned}\rho &= \rho^f + \mu(\rho^s - \rho^f) \\ \sigma_{ij} &= \sigma_{ij}^f + \mu(\sigma_{ij}^s - \sigma_{ij}^f) \\ e &= e^f + \mu(e^s - e^f)\end{aligned}\quad (2)$$

where the superscripts f and s denote the variables associated with fluid and solid, respectively,

$$\mu(\mathbf{x}) = \begin{cases} 0 & \mathbf{x} \in \Omega^f \\ 1 & \mathbf{x} \in \Omega^s \end{cases}\quad (3)$$

with Ω^f denoting the fluid region, Ω^s for the solid region and \mathbf{x} for the spatial coordinate in the current configuration.

The kinematic condition and boundary/initial conditions are given by

$$\dot{\epsilon}_{ij} = \frac{1}{2}(\dot{u}_{i,j} + \dot{u}_{j,i}) \tag{4}$$

$$n_j \sigma_{ji} = \bar{t}_i, \mathbf{x} \in \Gamma_t \tag{5}$$

$$u_i = \bar{u}_i, \mathbf{x} \in \Gamma_u \tag{6}$$

$$u_i(\mathbf{X}, 0) = u_{i0}(\mathbf{X}) \quad \dot{u}_i(\mathbf{X}, 0) = \dot{u}_{i0}(\mathbf{X}), \tag{7}$$

where Γ_u and Γ_t denote the displacement boundary and traction boundary of the material domain Ω , respectively, n_j is the unit normal of the boundary Γ_t , \mathbf{X} is the material coordinate, \bar{u}_i and \bar{t}_i are the prescribed displacement and traction, respectively, u_{i0} and \dot{u}_{i0} are the initial displacement and initial velocity, respectively.

The stress-rate of solid is related to the strain-rate by a constitutive equation as

$$\sigma_{ij}^{\nabla} = \sigma_{ij}^{\nabla}(\dot{\epsilon}_{ij}, \sigma_{ij}, \text{etc.}) \tag{8}$$

where

$$\sigma_{ij}^{\nabla} = \dot{\sigma}_{ij} - \sigma_{ik} \Omega_{jk} - \sigma_{jk} \Omega_{ik} \tag{9}$$

is the Jaumann rate of the Cauchy stress tensor,

$$\Omega_{ij} = (\dot{u}_{i,j} - \dot{u}_{j,i})/2 \tag{10}$$

is the spin tensor.

The Mie-Grüneisen type equation of state (EOS)

$$\rho e = f(\rho)p + g(\rho) \tag{11}$$

is used for fluid to close the governing equations, where ρ is the fluid density, e is the total energy per unit mass of the fluid, p is the fluid pressure, $f(\rho)$ and $g(\rho)$ are functions of fluid density. For example, for the ideal gas

$$f(\rho) = \frac{1}{\gamma - 1}, \quad g(\rho) = 0.0 \tag{12}$$

while for the products of high explosive

$$f(\rho) = \frac{1}{\omega}, \quad g(\rho) = -\frac{A}{\omega} \left(1 - \frac{\omega\rho}{R_1\rho_0}\right) \exp\left(-\frac{R_1\rho_0}{\rho}\right) - \frac{B}{\omega} \left(1 - \frac{\omega\rho}{R_2\rho_0}\right) \exp\left(-\frac{R_2\rho_0}{\rho}\right) \tag{13}$$

where A, B, R_1, R_2 and ω are the parameters of JWL EOS, ρ_0 is the initial density.

3. The MMALE particle method

Kan and Zhang [67] proposed a robust MMALE particle method for FSI problems. By immersing the MPM particles into the MMALE grid, the MPM and the MMALE method are strongly coupled as illustrated in Fig. 2.

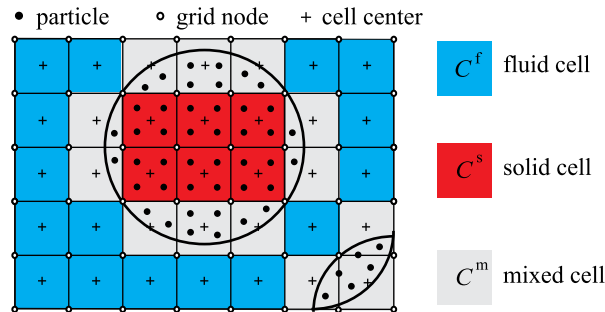


Fig. 2. The spatial discretization of the MMALE particle method.

The computational process of the MMALE particle method consists of a Lagrangian phase, a rezoning phase and a remapping phase. In the Lagrangian phase, the momentum equation is solved on the Lagrangian grid and the physical variables of fluid and solid are updated. The weak form equivalent to the momentum equation and traction boundary condition is given as

$$\int_{\Omega} \rho \ddot{u}_i \delta u_i d\Omega + \int_{\Omega} \rho \sigma_{ij}^s \delta u_{i,j} d\Omega - \int_{\Omega} \rho b_i \delta u_i d\Omega - \int_{\Gamma_t} \rho \bar{t}_i^s \delta u_i d\Gamma = 0 \tag{14}$$

where $\sigma_{ij}^s = \sigma_{ij}/\rho$ is the specific stress, $\bar{t}_i^s = \bar{t}_i/\rho$ is the specific traction, $\delta u_i \in \mathcal{R}_0(\mathcal{R}_0 = \{\delta u_i | \delta u_i \in C^0, \delta u_i|_{\Gamma_u} = 0\})$ is the virtual displacement. Substituting Eq. (2) into the weak form Eq. (14) and discretizing the problem domain with MMALE cells and MPM particles gives

$$m_I \dot{v}_{iI} = f_{iI} + f'_{iI}, \forall I \notin \Gamma_u \tag{15}$$

where f'_{iI} is the external force of node I ,

$$m_I = \sum_c \rho_c^f V_{cI} + \sum_p (\rho_p^s - \rho_p^f) V_p N_{Ip} \tag{16}$$

is the mass of node I , v_{iI} is the velocity of node I ,

$$\mathbf{f}_{iI} = \sum_c f_{ciI} - \sum_p V_p N_{Ip,j} (\sigma_{ijp}^s + P_p^f \delta_{ij}) \tag{17}$$

is the internal force of node I , the subscripts c and p denote the variables associated with the cell and particle respectively. In Eqs. (16) and (17), V_p is the volume of particle p , V_{cI} is the subcell [33] volume of cell c related to node I , N_{Ip} is the shape function of node I at particle p , P_p^f is the pressure of the virtual fluid located in the support domain of particle p , f_{ciI} is the fluid (including virtual fluid) part of the corner force applying on node I which is calculated with the pressure P_c^f stored at cell center as

$$f_{ciI} = -P_c^f \int_{\Gamma_I^c} n_i d\Gamma \tag{18}$$

For the multi-material cells, the pressure P_c^f is obtained with the Tipton pressure relaxation model [68].

After solving Eq. (15), the velocities and positions of the grid nodes are obtained. Then the state variables on the cell centers and particles are updated with respective ways of MMALE and MPM. The compatible discrete scheme [69,70] of the momentum and energy equation can preserve the total energy conservation and is adopted here by updating the cell energy as

$$m_c \frac{de_c}{dt} = - \sum_I f_{ciI} v_{iI} \tag{19}$$

where m_c and e_c are the mass and internal energy of the cell c respectively.

The predictor–corrector scheme [68] is used for the time integration where the variables are updated to the half time step to estimate the pressure and then the variables in the next time step will be updated. The velocity v_{iI}^{n+1} , $v_{iI}^{n+1/2}$ and displacement x_{iI}^{n+1} of the grid nodes are finally updated as

$$v_{iI}^{n+1} = v_{iI}^n + \dot{v}_{iI}^{n+1/2} \Delta t \tag{20}$$

$$v_{iI}^{n+1/2} = \frac{1}{2} (v_{iI}^n + v_{iI}^{n+1}) \tag{21}$$

$$x_{iI}^{n+1} = x_{iI}^n + v_{iI}^{n+1/2} \Delta t \tag{22}$$

With the idea of the constant parametric coordinate method [25], the velocity v_{ip}^{n+1} , $v_{ip}^{n+1/2}$ and displacement x_{ip}^{n+1} of solid particles are updated by interpolating the MMALE grid nodal velocities and displacements as

$$v_{ip}^{n+1} = v_{ip}^n + \Delta t \sum_{I=1}^8 \dot{v}_{iI}^{n+1/2} N_{Ip} \tag{23}$$

$$v_{ip}^{n+1/2} = v_{ip}^n + \frac{1}{2} \Delta t \sum_{I=1}^8 \dot{v}_{iI}^{n+1/2} N_{Ip} \tag{24}$$

$$x_{ip}^{n+1} = x_{ip}^n + \Delta t \sum_{I=1}^8 v_{iI}^{n+1/2} N_{Ip} \tag{25}$$

By this means, the fluid and solid are in the same velocity field and the no-slip interaction is realized naturally. Thus the MMALE particle method updates the strain and stress of the solid particles with the updated nodal velocity as

$$\Delta \epsilon_{ijp}^{n+1/2} = \sum_{I=1}^8 \frac{1}{2} (N_{Ip,j} v_{iI}^{n+1/2} + N_{Ip,i} v_{jI}^{n+1/2}) \Delta t \tag{26}$$

$$\Delta \Omega_{ijp}^{n+1/2} = \sum_{I=1}^8 \frac{1}{2} (N_{Ip,j} v_{iI}^{n+1/2} - N_{Ip,i} v_{jI}^{n+1/2}) \Delta t \tag{27}$$

$$\sigma_{ijp}^{n+1} = \sigma_{ij}^n (\sigma_{ijp}^n, \Delta \epsilon_{ijp}^{n+1/2}, \Delta \Omega_{ijp}^{n+1/2}) \tag{28}$$

However, as fluid and solid have great difference in compressibility, the velocities of nodes in the mixed cells may also differ greatly. When updated with the mixed FSI velocity field, spurious strain and stress of solid particles are induced and inaccurate

stress is caused in this way. Therefore, a decoupled stress updating scheme is presented in Section 4 to realize accurate calculation in the vicinity of FSI interface.

In the rezoning phase, the quality of seriously distorted grid is improved. Rezoning the grid to the initial one is adopted for the MMALE particle method which takes little CPU time and the natural coordinates of MPM particles in each cell can be easily determined. However, this treatment requires high computational cost in the remapping phase which transfers the physical variables to the new grid. The accurate polyhedron intersection based method [33,67] is adopted for its accuracy in multi-phase remapping which includes four steps: the reconstruction of multi-phase interface, linear reconstruction of physical field, polyhedron subdivision and intersection, and physical variables correction with solid particles. However with the global mesh rezoning, all cells in the new grid are intersected with the old one which is quite time-consuming. Therefore, a localized subdomain smoothing method is proposed in Section 5 to enhance the computational efficiency of the Euler phase (rezoning and remapping phase).

4. Decoupled stress updating scheme

Here a decoupled stress updating scheme for the Lagrangian phase of the MMALE particle method is presented based on a virtual grid of solid to realize accurate calculation in the vicinity of FSI interface. The solid grid is virtual as it is only adopted for updating the strain and stress of solid particles while the nodal mass and momentum of the real computational grid remain unchanged.

4.1. Process of the decoupled stress updating scheme

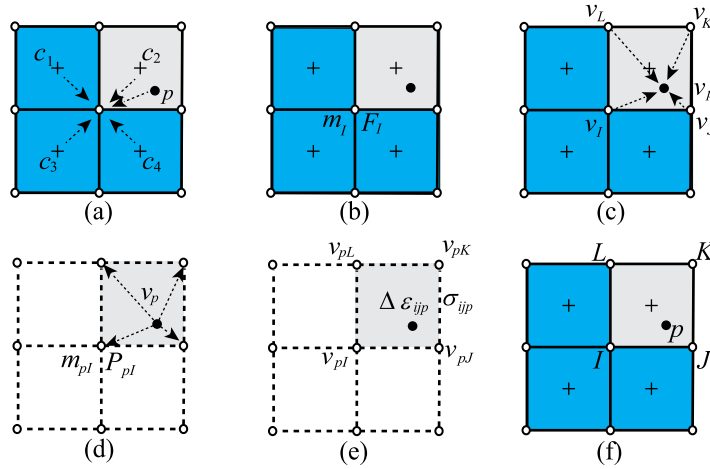


Fig. 3. Computational process of the decoupled stress updating scheme of the MMALE particle method: (a) nodal mass and force are obtained from both fluid and solid; (b) momentum equation is solved on the grid; (c) positions and velocities of nodes and particles are updated; (d) mass and momentum of the virtual grid are remapped from solid; (e) strain, vorticity and stress of solid are updated with the virtual grid; (f) virtual grid is abandoned and real grid is adopted for updating the fluid variables.

The computational process of the decoupled stress updating scheme is illustrated in natural coordinates so the positions of the particle and nodes remain unchanged in Fig. 3, which contains six steps as follows.

1. Calculate the nodal mass and nodal force from both solid and fluid with Eqs. (16) and (17) (Fig. 3(a)).
2. Update the momentum equation with the nodal force and mass by Eq. (15) (Fig. 3(b)).
3. Update the positions and velocities of the grid nodes and particles with Eq. (20)–(25) (Fig. 3(c)).
4. Remap the mass and momentum of each solid particle to the virtual grid nodes located in the same positions as the real grid nodes and apply the kinematic boundary conditions (Fig. 3(d)).

$$m_{Is} = \sum_p m_p N_{Ip} \tag{29}$$

$$m_{Is} v_{iIs}^{n+1/2} = \sum_p m_p v_{ip}^{n+1/2} N_{Ip} \tag{30}$$

where $v_{iIs}^{n+1/2}$ is the nodal velocity of the virtual grid at $n + 1/2$ time step.

5. Calculate the increments of strain and vorticity of each particle according to the newly calculated velocity of the virtual grid nodes as

$$\Delta \epsilon_{ijp}^{n+1/2} = \sum_{I=1}^8 \frac{1}{2} \left(N_{Ip,j} v_{iIs}^{n+1/2} + N_{Ip,i} v_{jIs}^{n+1/2} \right) \Delta t \tag{31}$$

$$\Delta \Omega_{ijp}^{n+1/2} = \sum_{I=1}^8 \frac{1}{2} \left(N_{Ip,j} v_{iIs}^{n+1/2} - N_{Ip,i} v_{jIs}^{n+1/2} \right) \Delta t \tag{32}$$

and update the stress of each particle with Eq. (28) (Fig. 3(e)).

6. Abandon the virtual solid grid and adopt the real grid after the solid variables are updated. The physical variables of the fluid are updated with the real grid as it represents the real velocity field of fluid with no-slip interaction of solid. (Fig. 3(f)).

$$V_c^{n+1} = V \left(x_i^{I,n+1} \right) \quad (33)$$

$$\rho_c^{n+1} = m_c / V_c^{n+1} \quad (34)$$

$$P_c^{n+1} = P \left(\rho_c^{n+1}, e_c^{n+1} \right) \quad (35)$$

In step 4, a velocity field of solid is obtained, which is more accurate to update the strain and vorticity of particles as it removes the influence of fluid velocity. When Step 4 is omitted and the nodal velocity in real grid is adopted for updating the strain and vorticity in Step 5, the decoupled stress updating scheme degenerates to the original stress updating scheme.

Remark 1. Although the weak coupling of FSI in which the fluid offers the forces to the solid and the solid provides the displacement boundary for the fluid can be employed for the MMALE particle method, it loses the advantage of calculating the momentum equations of fluid and solid in the same grid and time step. The momentum equations of fluid and solid are solved alternately and force and displacement boundaries cannot be guaranteed in a whole time step.

4.2. Theoretical analysis

A special situation is considered here. When the node I is influenced by only one particle p as shown in Fig. 3(a), the nodal mass and nodal force can be expressed as

$$m_I = m_p N_{Ip} - m'_p N_{Ip} + m_{IC} \quad (36)$$

$$f_{iI}^{n+1/2} = f_{iIC}^{n+1/2} - N_{Ip,j} \left(\sigma_{ijp}^{n+1/2} + P_p^{n+1/2} \delta_{ij} \right) V_p \quad (37)$$

where m_p is the mass of particle p , m_{IC} is the mass of real and virtual fluid in the control volume of node I , m'_p and $P_p^{n+1/2}$ are the mass and pressure of the virtual fluid occupied by particle p respectively.

Substituting Eqs. (36) and (37) into

$$v_{iI}^{n+1/2} = \frac{P_{iI}^{n+1/2}}{m_I} = \frac{P_{iI}^n + \frac{1}{2} f_{iI}^{n+1/2} \Delta t}{m_I} \quad (38)$$

gives

$$\begin{aligned} v_{iI}^{n+1/2} &= \frac{P_{iI}^n}{m_I} + \frac{1}{2} \Delta t \frac{f_{iI}^{n+1/2}}{m_p N_{Ip} - m'_p N_{Ip} + m_{IC}} \\ &= v_{iI}^n + \frac{1}{2} \Delta t \frac{f_{iIC}^{n+1/2} - N_{Ip,j} \left(\sigma_{ijp}^{n+1/2} + P_p^{n+1/2} \delta_{ij} \right) V_p}{m_p \left(N_{Ip} + \frac{m_{IC} - m'_p N_{Ip}}{m_p} \right)} \end{aligned} \quad (39)$$

When the particle is approaching the cell boundary away from the node I , $N_{Ip} \rightarrow 0$,

$$m_I = m_p \left(N_{Ip} + \frac{m_{IC} - m'_p N_{Ip}}{m_p} \right) \rightarrow m_{IC} \quad (40)$$

but $N_{Ip,j} \neq 0$. Thus the velocity $v_{iI}^{n+1/2}$ used to update the strain and vorticity of the solid particle is actually calculated with the coupled nodal force, the nodal mass of fluid and the nodal velocity v_{iI}^n which is an average of solid and fluid velocity, as

$$v_{iI}^{n+1/2} \rightarrow v_{iI}^n + \frac{1}{2} \frac{f_{iI}^{n+1/2}}{m_{IC}} \Delta t \quad (41)$$

The density and compressibility of the fluid and solid are of great difference and the velocity $v_{iI}^{n+1/2}$ may be quite different from the actual velocity of solid. When an overestimated velocity $v_{iI}^{n+1/2}$ is used to determine the strain and vorticity of solid particles by Eqs. (26) and (27), the strain, vorticity and stress are also overestimated compared to the real ones. If the solid particle moves across the cell boundary and into the solid cell in the next timestep, the new nodal mass m_j is composed of both solid and fluid and thus the nodal velocity for updating the strain and vorticity of particles is actually an weighted average of the solid and fluid velocity. The strain and stress of the same particle differ greatly in the consecutive time steps and stress oscillation may occur.

With the use of the decoupled updating scheme, a virtual grid with solid mass and velocity field is acquired. The mass of the node I in the virtual grid is only related to mass of particle p and Eq. (29) is now expressed as

$$m_{Is} = m_p N_{Ip} \quad (42)$$

The nodal velocity $v_{iIs}^{n+1/2}$ of the virtual grid is updated as

$$v_{iIs}^{n+1/2} = \frac{p_{iIs}^{n+1/2}}{m_{Is}} = \frac{m_p N_{Ip} v_{ip}^{n+1/2}}{m_p N_{Ip}} = v_{ip}^{n+1/2} \quad (43)$$

The velocity of the particle $v_{ip}^{n+1/2}$ is calculated with Eq. (24) in Step 3 and Eq. (43) can be expressed as

$$\begin{aligned} v_{iIs}^{n+1/2} &= v_{ip}^n + \frac{1}{2} \Delta t \sum_{J=1}^8 \dot{v}_{iJ}^{n+1} N_{Jp} \\ &= v_{ip}^n + \frac{1}{2} \Delta t \sum_{J=1}^8 \frac{f_{iJ}^{n+1/2} N_{Jp}}{m_J} \end{aligned} \quad (44)$$

Substituting Eq. (36) into Eq. (44), we obtain

$$v_{iIs}^{n+1/2} = v_{ip}^n + \frac{1}{2} \Delta t \sum_{J=1}^8 \frac{f_{iJ}^{n+1/2} N_{Jp}}{m_p N_{Jp} - m'_p N_{Jp} + m_{JC}} \quad (45)$$

The numerator and denominator of the second term in Eq. (45) are both related to the shape function N_{Jp} . When a particle is near the boundary of a cell, $N_{Jp} \rightarrow 0$ and $\frac{f_{iJ}^{n+1/2} N_{Jp}}{m_p N_{Jp} - m'_p N_{Jp} + m_{JC}} \rightarrow 0$ which means the nodes far from the particles and near the fluid have little influence on the velocity $v_{ip}^{n+1/2}$ and $v_{iIs}^{n+1/2}$. As strong FSI coupling is realized in ALEPM by immersing the particles in the MMAL cells, fluid and solid are in the same velocity field with the no-slip interaction. The velocity of the particle represents the actual velocity of solid in the computational grid and therefore the nodal velocity $v_{iIs}^{n+1/2}$ determined by Eq. (43) reflects the actual velocity field of solid. The influence of the fluid velocity in the mixed velocity field $v_{iI}^{n+1/2}$ calculated by Eq. (38) is eliminated in this way and thus the strain, vorticity and stress calculated by Eq. (31), Eq. (32) and Eq. (28) are actual strain, vorticity and stress of the solid, which is more accurate than the original stress updating scheme. In the next timestep, the nodal forces calculated by Eq. (17) are updated with correct solid stress σ_{ijp}^s and therefore accurate FSI coupling is applied on the fluid.

5. Localized subdomain smoothing method

Localized smoothing is appropriate to realize efficient remapping and enhance the overall computational efficiency. A localized subdomain smoothing method (LSSM) is presented in the principle of the following requirements: (a) great performance in the mesh quality; (b) low computational cost itself; and (c) localized enough for less intersection calculation, and consists of a distorted subdomain determination step and a combined mesh smoothing step.

5.1. Mesh quality inspection

Mesh quality inspection is conducted after a Lagrangian phase to determine whether the grid needs rezoning. The maximum ratio of side lengths and largest inclined angle related to the cell shape [71], as well as the average nodal displacement between two Lagrangian steps [34], can be used to judge whether the grid is distorted. The rezoning and remapping phases are not conducted until the grid is determined distorted after several Lagrangian steps. Then a universal criteria [45,72] defined by the geometry quantities (such as cell volume, surface area and sum of side lengths) is introduced for the unity to judge the quality Q_l of each cell c_l as

$$Q_l = \begin{cases} \frac{1728V_l}{L_l^3}, & \text{for 3D cells} \\ \frac{16S_l}{L_l^2}, & \text{for 2D cells} \end{cases} \quad (46)$$

where l is the cell index, V_l is the volume of the 3D cell, S_l is the area of the 2D cell, L_l is the sum of side lengths. The quality Q_l defined by Eq. (46) varies with the changes of both cell angle and side length which are related to the critical time step size. When cell c_l is a regular hexahedron or quadrilateral, Q_l equals to 1.

5.2. Distorted subdomain determination step

Inspired by the idea of adaptive mesh refinement (AMR), a distorted subdomain determination step is proposed to automatically identify the distorted areas of the grid as shown in Fig. 4. Each subdomain is enlarged from a single distorted cell and finally covers

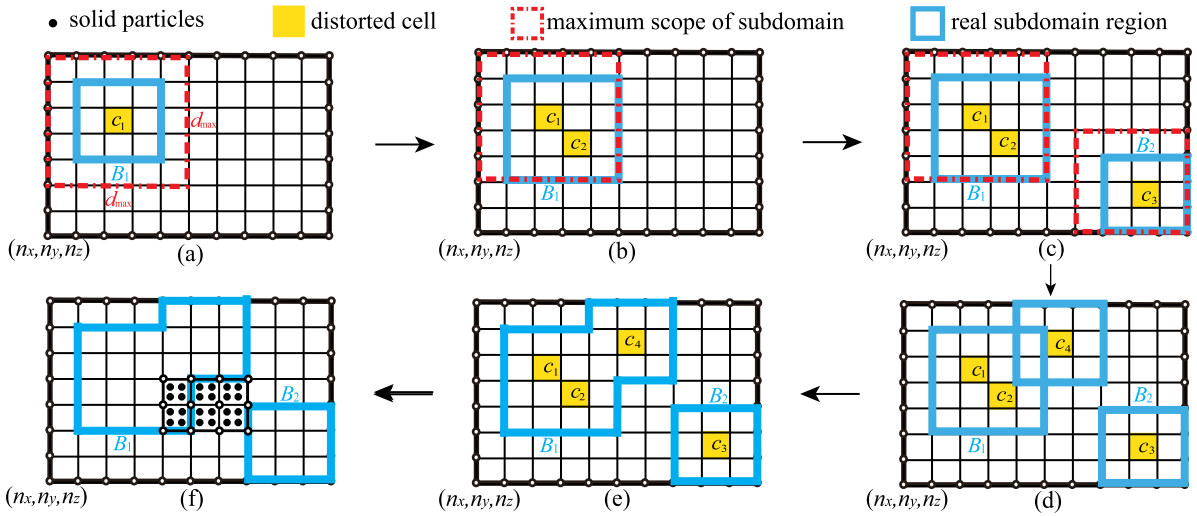


Fig. 4. Computational process of the distorted subdomain determination step: (a) the first subdomain is obtained with surrounding cells of the first distorted cell; (b) the subdomain is enlarged if a subsequent distorted cell is within the maximum range of an existing subdomain; (c) a new subdomain is established when a subsequent distorted cell is not within the maximum range of any subdomain; (d) all subdomains are obtained and may be overlapped with each other; (e) the overlapped subdomains make up of a step-like subdomain; (f) regular cells occupied by the particles are marked as fixed boundary of the grid.

the area of $[l_{xmin}, l_{xmax}] \times [l_{ymin}, l_{ymax}] \times [l_{zmin}, l_{zmax}]$ where l_x, l_y and l_z are respectively the index of cell c_l in x -, y - and z -direction of the structured grid. Note that Fig. 4 is illustrated in 2D grids for clarity and the step is actually applicable for 3D grids with the following computational process.

(Cell loop)

1. Compute the quality Q_l of cell c_l with Eq. (46) and mark the cell as distorted if the quality criterion $Q_l < q$ is satisfied, where q is the prescribed quality parameter of distorted cells.
2. Insert each distorted cell into a subdomain according to different situations

(a) For the first distorted cell,

- i. Set the first subdomain B_1 to be the surrounding cells (9 cells for 2D grids and 27 cells for 3D grids) of the distorted cell at first as shown in Fig. 4(a).
- ii. Set the center of the first subdomain to be (l_x, l_y, l_z) and set the maximum range of subdomain B_1 with the center (l_x, l_y, l_z) and the maximum side length d_{max} .

(b) For subsequent distorted cells,

- i. (Subdomain loop) Expand the existing subdomain B_k (k is the index of subdomain) to cover the surrounding cells of c_l if cell c_l is within the maximum range of B_k as illustrated in Fig. 4(a)(b)(c). The center of subdomain B_k remains unchanged.
- ii. Set a new subdomain B_k to be the surrounding cells of cell c_l if c_l is not within the maximum range of any existing subdomain. Set the subdomain center to be (l_x, l_y, l_z) and the maximum range of subdomain B_k as shown in Fig. 4(c).

3. Expand all subdomains in each direction to get a smoother boundary without distorted cells.

The maximum side length d_{max} of the subdomain is determined according to the scale and type of the problem. As illustrated in Fig. 5, too large subdomains may include too many cells without distortion while too small subdomains are probably all overlapped and thus distorted cells are smoothed for many times in one iteration, which will both reduce the smoothing efficiency. In this article, the d_{max} is taken as 1/10 of the minimum side length in the 2D/3D grid.

After the cell loop, all distorted cells are placed into the subdomains which are probably overlapped with each other and an irregular smoothing area is formed as shown in Fig. 4(d). However the overlapped subdomains need no special treatment as they compose a step-like subdomain whose boundary cells are in good quality, as illustrated in Fig. 4(e).

Remark 2. In the MMALE particle method, rezoning of the subdomains with solid particles requires determination of the new cells in which particles are located and the corresponding new natural coordinates, which is time-consuming and may cause imprecision. Therefore, a pre-positioning method is realized in which the physical coordinates of the particles are used to determine which cells of the standard orthogonal grid the particles should be in. Once the regular cells are determined, the natural coordinates of particles

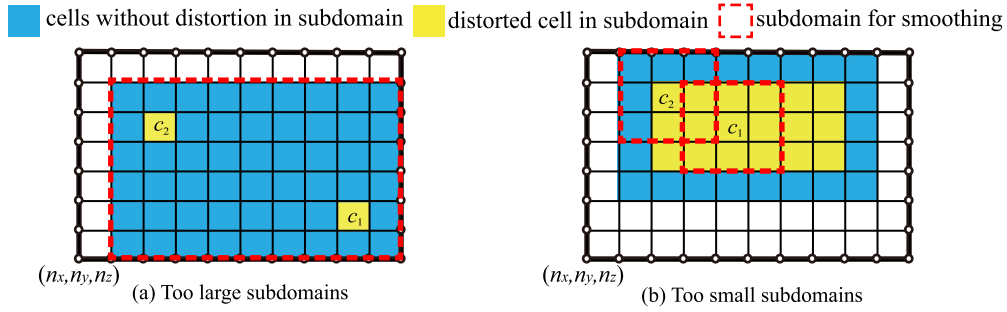


Fig. 5. Inappropriate sizes of subdomains which affects the smoothing efficiency and results.

are obtained. During the subsequent mesh smoothing process, the cells occupied by the particles remain unchanged and are seen as the fixed inner boundary of the grid, as illustrated in Fig. 4(f).

5.3. Combined mesh smoothing step

As mentioned before, each smoothing method has its own drawbacks and no method can be feasible for all situations. Therefore a combined mesh smoothing step is proposed with the modified GETMe, the weighted average method [56] and the transfinite interpolation method [73].

5.3.1. The modified GETMe

Firstly the GETMe is modified to achieve higher efficiency and better untangling capabilities in structured orthogonal grid. The GETMe firstly transforms each cell of the grid to a more regular one [50] with the cell centroid unchanged. The centroid x_{c_i} of each cell c_i is obtained as

$$x_{c_i} = \frac{1}{m} \sum_{k=1}^m x_{I_{ik}} \tag{47}$$

where $x_{I_{ik}}$ is the position of the k th node in cell c_i , m equals to 4 for 2D cells and 8 for 3D cells. The estimated positions of the nodes in cell c_i are calculated according to the octahedron which is determined by connecting the centroids of the eight cell surfaces, as shown in Fig. 6

$$x'_{I_{ik}} = x_{o_{I_{ik}}} + \frac{b}{\sqrt{|n_{I_{ik}}|}} n_{I_{ik}}, \quad k \in \{1, \dots, 8\} \tag{48}$$

where $x'_{I_{ik}}$ is the new nodal positions of the transformed hexahedron, $x_{o_{I_{ik}}}$ is the position of the centroid $o_{I_{ik}}$ on the k th dual octahedron surface, $n_{I_{ik}}$ is the associated normal of the k th dual octahedron surface, $b \in \mathbb{R}^+$ is a arbitrary scaling factor for regularizing transformation of the cell.

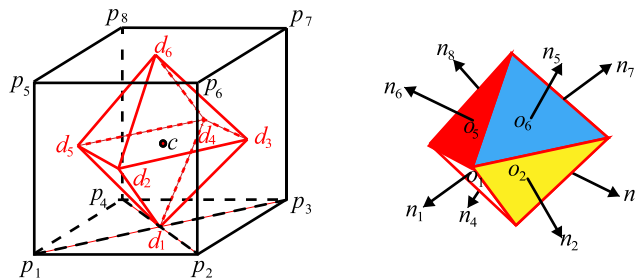


Fig. 6. Single cell transformation with an octahedron in GETMe [50].

The new cell is then thrunk to preserve its initial volume or sum of side lengths as

$$x''_{I_{ik}} = x_{c_i} + \frac{\sqrt[3]{V'_i}}{\sqrt[3]{V_i}} (x'_{I_{ik}} - x_{c_i}), \quad \text{or} \quad x''_{I_{ik}} = x_{c_i} + \frac{L'_i}{L_i} (x'_{I_{ik}} - x_{c_i})$$

where V'_i is the current volume of the cell c_i and L'_i is the current sum of side lengths. As each node is related to its surrounding cells, the nodal position is finally determined as the average of all joint cells. The GETMe transformation is proved invariant with respect to translation, rotation and scaling and can preserve the centroid of the initial hexahedron. For unstructured meshes, this invariance will help maintain the overall mesh topology. However, as the structured orthogonal grid with hexahedral cells is mainly

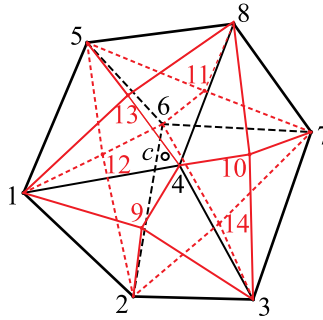


Fig. 7. Division of a hexahedral cell with nodes, side centers, surface centers and cell center [33].

adopted in the MMALE particle method, a modified GETMe is presented with determination of the cell centroid in a more accurate way and changing the geometric deformation process to eliminate the effect of rotation.

In ls-ALEPM, each hexahedral cell splits into 24 tetrahedrons for intersection by connecting the cell nodes, side centers, surface centers and volume center as illustrated in Fig. 7. Thus more accurate cell centroid is obtained by adding the moment of volume of all these tetrahedrons divided by cell volume as

$$x_{c_l} = \frac{1}{V_l} \sum_{k=1}^{24} x_{t_{lk}} V_{t_{lk}} \tag{49}$$

where $x_{c_{lk}}$ and $V_{t_{lk}}$ are the centroid and volume of the tetrahedron t_{lk} respectively.

For the cell geometric deformation process, a rotation step is added as the sides of an optimal cell are parallel or perpendicular to the three axes of Cartesian coordinate system. Transforming the cells into cubes of standard grid whose side length is the average of cell side lengths as $\bar{a} = \frac{1}{12} \sum_{i=1}^{12} a_i$, the new position of each grid node is obtained by

$$x_k = x_{c_l} + \frac{1}{2} \bar{a} \begin{pmatrix} A_{1k} \\ A_{2k} \\ A_{3k} \end{pmatrix}, \text{ where } [A_{ij}] = \begin{bmatrix} -1 & 1 & 1 & -1 & -1 & 1 & 1 & -1 \\ -1 & -1 & 1 & 1 & -1 & -1 & 1 & 1 \\ -1 & -1 & -1 & -1 & 1 & 1 & 1 & 1 \end{bmatrix} \tag{50}$$

As illustrated in Fig. 8, the cell obtained by GETMe can be transformed into cubes without inclined angle while the cell obtained by GETMe is still inclined after the cell geometric deformation. Then the final node position is determined by calculating the average position of nodes in the adjacent cells.

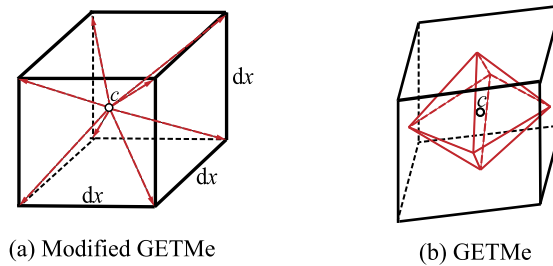


Fig. 8. Comparison of single cell transformation in modified GETMe and GETMe.

As the cells in standard orthogonal grids should be regular hexahedra with the same size, the presented modified GETMe accelerates the smoothing of structured orthogonal grids as the cells (even illegal cells) can be regularized into a cube in only one iterative step. However, cells in the GETMe cannot be transformed into cubes even after many iterations. The modified GETMe is also applicable for 2D cells by calculating cell centers with Eq. (47) and updating the new positions as

$$x_k = x_{c_l} + \frac{1}{2} \bar{a} \begin{pmatrix} A_{1k} \\ A_{2k} \\ 0 \end{pmatrix}, \text{ where } [A_{ij}] = \begin{bmatrix} -1 & 1 & 1 & -1 \\ -1 & -1 & 1 & 1 \end{bmatrix} \tag{51}$$

5.3.2. The combined mesh smoothing

A combined mesh smoothing step is developed to rezone the subdomains and consists of two processes. Firstly the modified GETMe and the weighted average method are used together to smooth the subdomains in each iteration step. The maximum number of iterations N_{max} is artificially preset and the iteration process is terminated when the quality criterion is satisfied. The transfinite interpolation method is introduced as a supplementary process to guarantee the grid quality if the quality criterion is still not satisfied after prescribed maximum number of iterations. The whole process is illustrated in Fig. 9 and is summarized as follows.

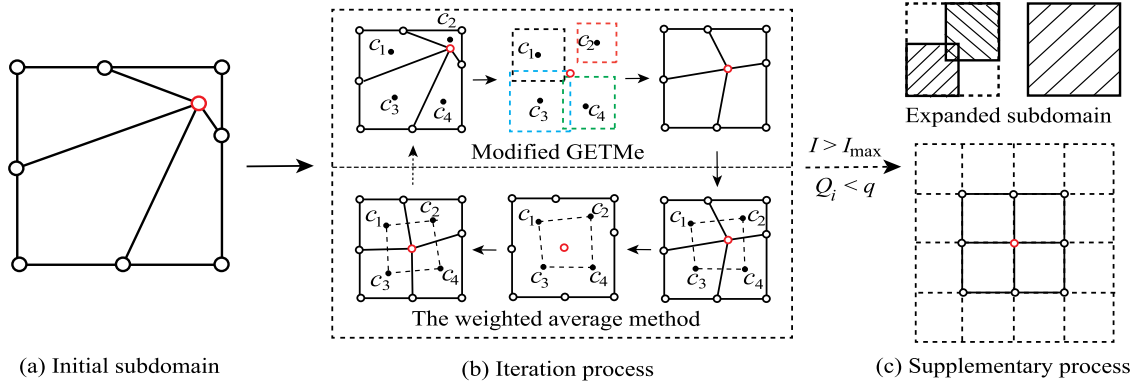


Fig. 9. Process of the combined mesh smoothing step.

1. Conduct the iteration process composed of the GETMe smoothing and weighted average method smoothing in the localized subdomains (Fig. 9(b)).
 - (a) Conduct one iteration of the GETMe smoothing.
 - (b) Conduct one iteration of the weighted average method smoothing.
 - (c) Judge if the objective grid quality criterion $Q_{\min} \geq q$ is satisfied after each iteration where Q_{\min} is the worst cell quality of the grid. If $Q_{\min} \geq q$, the whole process is finished and the supplementary process is not conducted.
 - (d) Judge if the iteration number N reaches the prescribed maximum number of iterations N_{\max} . If $N > N_{\max}$, the iteration process is finished and the supplementary process is conducted.
2. Conduct the supplementary process with the transfinite interpolation method (Fig. 9(c)).
 - (a) Merge the overlapped subdomains into larger cuboid subdomains.
 - (b) Conduct the transfinite interpolation method smoothing in non-overlapping subdomains.

During the iteration process shown in Fig. 9(b), the nodes located at the boundary surfaces of the 3D grids are smoothed as the way in 1D/2D grids in the iteration process. When located at the inner part of boundary surface, the nodes are updated with Eqs. (51) and (52). And when located at the edge of boundary surface, the nodes are updated as the arithmetic average while corner nodes are located at the initial position.

The modified GETMe transforms each cell into a cube and thus quickly improve the quality of severely distorted cells in early iteration steps. However Q_I defined by Eq. (46) grows slowly with the iteration when the grid is nearly regular. Therefore the weighted average method is adopted for its simplicity and effectiveness to deal with the grid in good quality. The cell center is given as Eq. (47) and the new position of an inner node I can be calculated as

$$x_I = \frac{\sum_k S_k x_{c_k}}{\sum_k S_k} \tag{52}$$

where S_k represents the area of the cell for 2D or volume of the cell for 3D problems, x_{c_k} is the center of the surrounding cell c_k . Combination of the two methods can make use of their advantages and thus enhance the capacity of smoothing method.

In the supplementary process shown in Fig. 9(c), the transfinite interpolation method recovers the quality of grid for the next Lagrangian phase. The overlapped subdomains are merged and expanded into cuboid subdomains whose boundaries are ensured to be relatively regular. The new nodal positions are calculated according to the boundary nodes of the subdomains as

$$x_I = \sum_J K_{IJ} x_J \tag{53}$$

where x_J is the position of the boundary node J , K_{IJ} is the scaling factor related to the distance from node I to related boundary node J . Obviously, this method is computationally efficient, but it is only applicable to grids with regular distribution of boundary nodes as cells of low quality may be generated with irregular boundary, as shown in Fig. 10. Through the transfinite interpolation method, the quality of the newly generated grid is guaranteed and the robustness of the combined mesh smoothing step is enhanced. The Euler phase with the transfinite interpolation method adopted is still more efficient than the original global rezoning MMALE particle method as only localized regions are involved in the smoothing.

So far the combined mesh smoothing step has been realized, which is not only applicable to the MMALE/MMALE particle method but also to any other Lagrangian methods with structured grids.

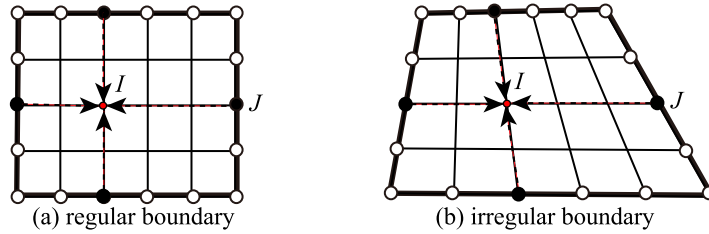


Fig. 10. Comparison of smoothing effects with regular and irregular boundary for transfinite interpolation method.

5.4. Remapping with the LSSM

Unlike the global remapping in which all cells in the new grid are intersected with the old grid, cells in ls-ALEPM are classified as subdomain cells and unchanged cells with the adoption of LSSM in which only subdomain cells are remapped. As the staggered ALE [14,33,67] is adopted in which the state variables like the mass, volume and internal energy of the cell are stored in the cell center while the kinematics and kinetics variables like the momentum and velocity are stored on the grid nodes. The control volume C_l of the new cell c_l is composed of $\Omega_{c_l}^{I_1}$, $\Omega_{c_l}^{I_2}$, $\Omega_{c_l}^{I_3}$ and $\Omega_{c_l}^{I_4}$ while the control volume D_j of node I_j is composed of $\Omega_{c_1}^{I_j}$, $\Omega_{c_2}^{I_j}$, $\Omega_{c_3}^{I_j}$ and $\Omega_{c_4}^{I_j}$ as illustrated in Fig. 11.

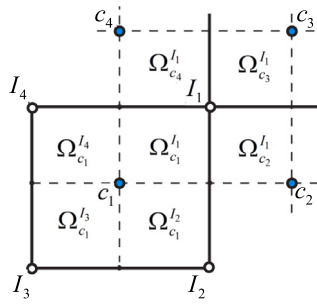


Fig. 11. Different control volume of cells and nodes in staggered MMALE [67].

The remapping with the LSSM also adopts the polyhedron intersection based method [33,67] to accurately deal with the multiphase FSI problems. For state variables stored in the cell centers, unchanged cells copy the old variables while cells in the newly generated grid intersect with the subdomain cells and their new variables are obtained by summing the related intersection fragments. The MoF method is used to reconstruct the material surface in MMALE cells of the old grid with the volume fraction and centroid of different materials, which is proved robust and correct in multiphase flow situations such as bubbles and detonation [22,67,74–76]. Then the cells are subdivided into single-material polyhedrons with the planar material surface as illustrated in Fig. 12.

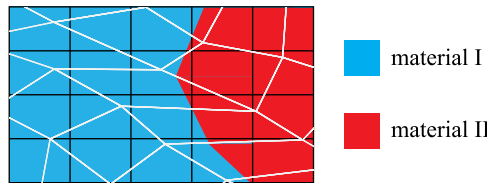


Fig. 12. Diagram of polyhedron subdivision and intersection.

Meanwhile each new cell in rezoned localized areas is divided into 24 tetrahedrons with the cell center, nodes and centers of the cell faces and is represented by 24 triangle pieces decomposed from the six cell surfaces as shown in Fig. 7. With the modified “clipping and capping” algorithm [33], the tetrahedrons are intersected with the single-material polyhedrons and the intersection fragments inside the new control volume can be acquired precisely with no matter convex subdivision, non-convex subdivision and multiple subdivision. For example, the volume of the k th material in the new cell is obtained by summing the intersection fragments in the control volume C_l as

$$V_k(c_l) = \sum_n V(C_l \cap Q_k^n), n \in \{n | C_l \cap Q_k^n \neq \emptyset\} \tag{54}$$

where Q_k^n denotes the k th material polyhedron in n th cell of the old grid. Then the total volume of the cell c_l is obtained as

$$V(c_l) = \sum_k V_k(c_l) \tag{55}$$

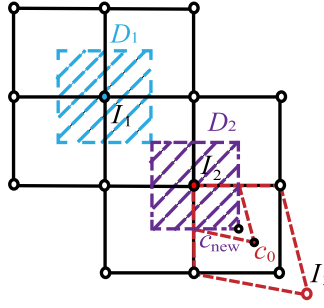


Fig. 13. Remapping of the kinematics and kinetics variables stored on the nodes which are related to all surrounding cells.

However, remapping of the kinematics and kinetics variables need special handling as grid nodes located at the interface of the subdomains may be related to both subdomain cells and unchanged cells. As shown in Fig. 13, the cell c_0 is marked to be distorted and thus the node I_3 of c_0 is relocated, making the control volume D_2 and nodal momentum of node I_2 changed. As the cells related to D_2 may be multi-phase, interpolating the nodal momentum from the adjacent nodes is inaccurate and incompatible.

Here the accurate remapping is realized by expanding each localized subdomain by only one layer of cells in the remapping phase, and therefore the outermost nodes of the subdomains and their control bodies remain unchanged in the previous rezoning phase. When cells in the expanded subdomains are intersected with the old grid, the nodal variables stored on the outermost nodes such as I_1 can copy their original nodal momentum. This treatment is accurate and still efficient as subdomains are usually small compared with the whole grid.

The momentum of the k th material stored on the node I_j is calculated by summing the intersection fragments in the nodal control volume D_j as

$$M_k(I_j) = \sum_n M(D_j \cap Q_k^n), n \in \{n \mid D_j \cap Q_k^n \neq \emptyset\} \quad (56)$$

Then the total momentum stored on the node I_j is obtained as

$$M(I_j) = \sum_k M_k(I_j) \quad (57)$$

6. Flowchart of the ls-ALEPM

So far we have presented a decoupled stress updating scheme to improve the accuracy of Lagrangian phase and a localized subdomain smoothing method to increase the efficiency of the Euler phase in the MMALE particle method. The flowchart of the localized subdomain smoothing MMALE particle method (ls-ALEPM) is illustrated in Fig. 14.

7. Numerical results

7.1. Smoothing benchmark of 3D distorted grid

A cuboid grid composed of $50 \times 50 \times 50$ distorted cells is considered here and shown in Fig. 15. The grid is used to verify the ability of the LSSM in dealing with severely distorted grids and is generated by moving a random distance from the position in the orthogonal standard grid. The distance between adjacent nodes in the standard orthogonal grid is 1 and the range of the random displacement in each direction is within $[-0.399, 0.399]$. In this way, the grid is in poor quality with the worst cell quality of 0.3010 determined by Eq. (46) but without illegal cells.

The GETMe, weighted average method, modified GETMe and combined smoothing method are used to smooth all cells of the grid and the objective grid quality criterion is set to be $Q_{\min} > 0.9999$. The combined smoothing method is composed of the modified GETMe and the weighted average method as in Section 5.3 while the transfinite interpolation method is not adopted. The worst cell quality Q_{\min} of the grid versus the CPU time t is illustrated in Fig. 16 as well as the cell shape according to the quality parameters. All the CPU time is measured on a computer with an Intel(R) Core™ i9-11900K CPU (3.50 GHz) and 64 bit Windows operating system. The modified GETMe performs much better than the GETMe and converges to 0.9999 after 52 iteration steps. The GETMe does not converge to 0.9999 after 100 iteration steps and fluctuates at 0.95. The weighted average method and the combined method both reaches the final convergence value of 0.9999 and the combined smoothing method shows its superiority.

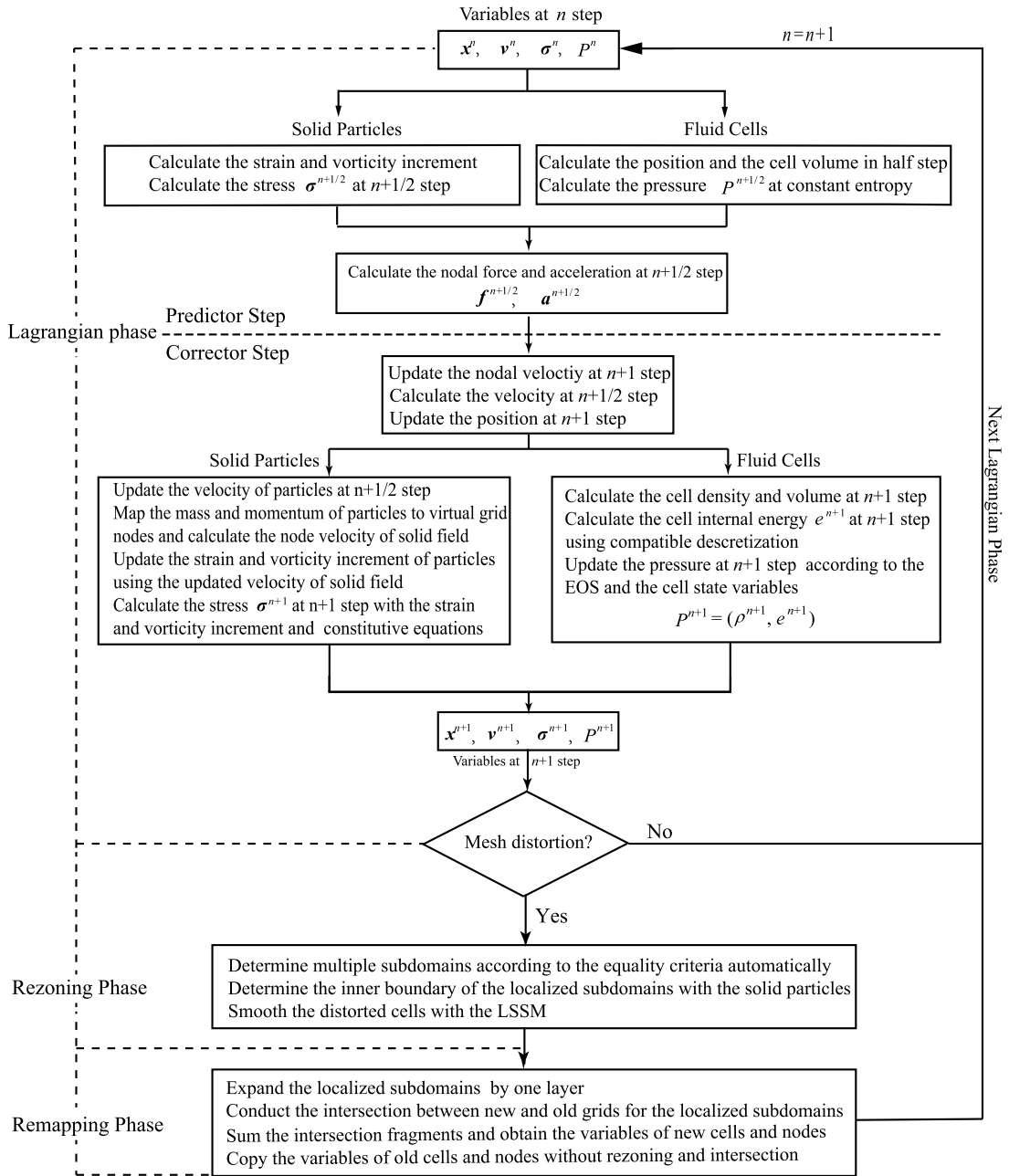


Fig. 14. Flowchart of the novel ls-ALEPM method.

7.2. Two-material sod problem

A multiphase Sod problem described in [24,68,77] is studied here to compare the accuracy of the proposed ls-MMALE method with MMALE and other methods. The computational domain is [0, 1] with the initial material interface at $x = 0.5$. The initial conditions for the left and right materials are $(\rho_l, P_l, U_l, \gamma_l) = (1, 2, 0, 2)$ and $(\rho_r, P_r, U_r, \gamma_r) = (0.125, 0.1, 0, 1.4)$ respectively with different polytropic indices. The computational grid is made of $N = 100$ cells and the final time is $t_{final} = 0.2$. This results simulated with the HWENO DG scheme [78] and Lagrangian scheme cell-centered MMALE method with 100 cells in the x -direction [24] are also shown in Fig. 17, which serves as comparison methods with ls-MMALE. The Euler step is conducted per 0.04 and the quality criterion for determining the distorted cells in ls-MMALE is set to be $Q_l < 0.75$. The numerical results including density and pressure distributions at $t_{final} = 0.2$ with different methods are illustrated in Fig. 17 as well as the analytical solution.

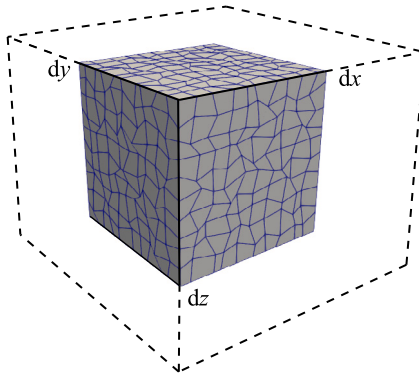


Fig. 15. Diagram of the 3D grid with distorted cells.

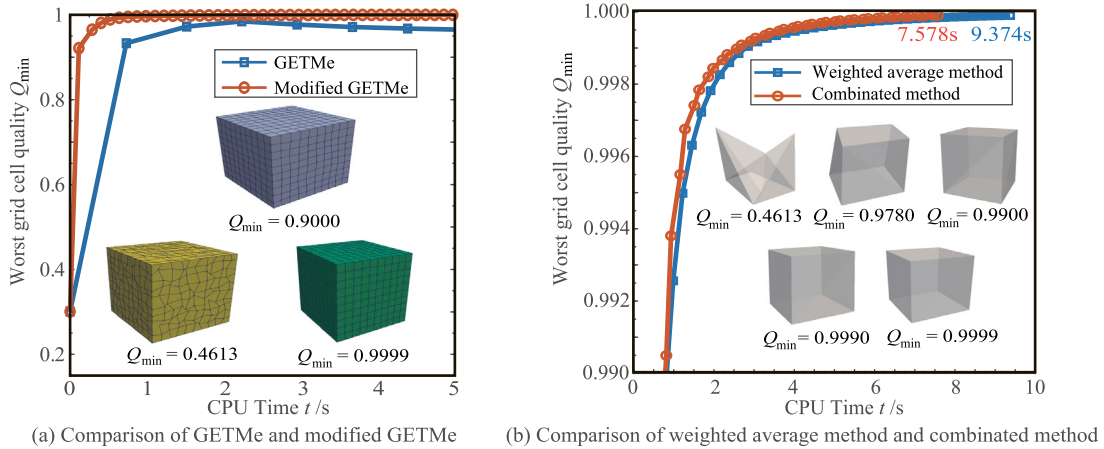


Fig. 16. The worst cell quality versus the CPU time with the GETMe, modified GETMe, weighted average method and combined smoothing method.

As shown in Fig. 17, the magnitudes and locations of oscillation in ls-MMALE are different from the HWENO DG scheme and Lagrangian scheme cell centered MMALE method as the staggered ALE scheme is adopted which is accurate and robust while the DG method is not used. By comparing with the analytical solution, the ls-MMALE achieves closer results in Fig. 17(a)(b).

The density and pressure curves at $t_{final} = 0.2$ simulated by ls-MMALE and MMALE with $N = 1000$ cells are illustrated Fig. 17(c)(d). With mesh refinement, all the distribution curves are in good agreement with the analytical solution. However, more spurious oscillations are observed with the MMALE method and the numerical results of the ls-MMALE are closer to the analytical solution. As the rezoning and remapping phases are conducted only in localized areas of the computational grid in ls-MMALE, less numerical remapping errors are introduced and the physical variables updated by the Lagrangian phase are maintained. Therefore, accuracy gains can also be obtained with the localized subdomain smoothing method.

7.3. Sedov point explosion problem

Next the problem of Sedov point explosion is studied to test the computational efficiency and the accuracy of the ls-MMALE. The Sedov point explosion simulates the shock wave propagation phenomenon caused by the point explosion of ideal gas and the analytical solution of the problem is available.

The computation model is shown in Fig. 18 with the computational domain $[0, 1.2] \times [0, 1.2] \times [0, 1.2]$ discretized into $40 \times 40 \times 40$ hexahedral cells in the structured grid. All cells are filled by the ideal gas with the polytropic index $\gamma = 1.4$, the initial density $\rho_0 = 1$ and initial velocity $U_i = 0$. The internal energy of the whole domain is initially concentrated at the origin cell whose pressure P_0 is given by

$$P_0 = (\gamma - 1)\rho_0 \frac{E_0}{V_0} \tag{58}$$

where E_0 is 0.244816[75], and V_0 denotes the volume of the origin cell. The pressure of the other cells is 1×10^{-6} . After the explosion, high pressure gas at the origin cell push the ideal gas outward and shock discontinuity is captured. When physical time $t = 1$, the shock front is located at $R = 1$ and the peak density $\rho = 6$ in the analytical solution.

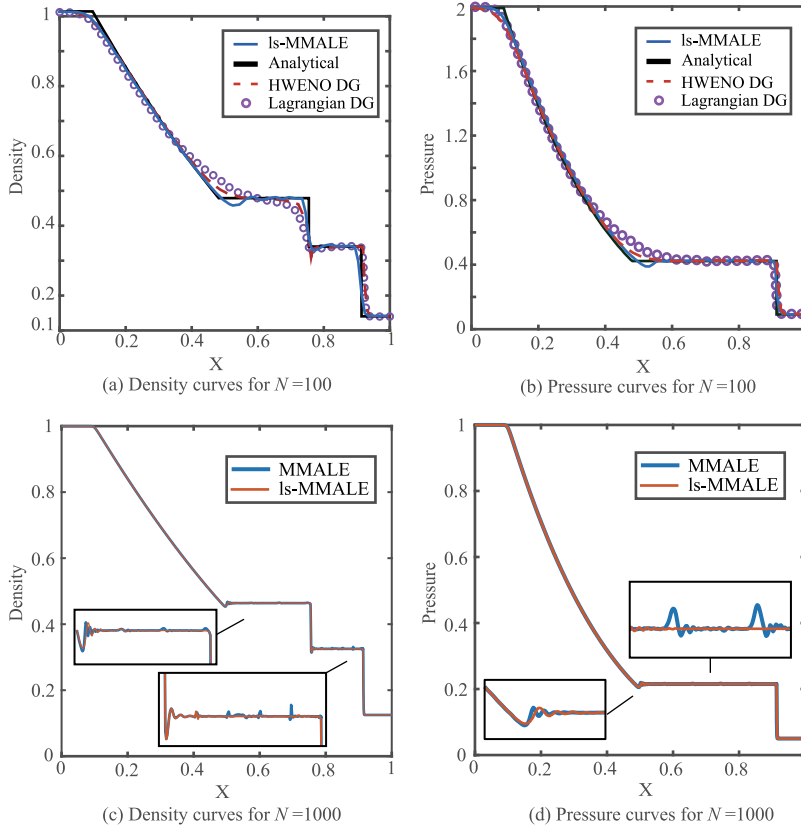


Fig. 17. Density and pressure curves of two-material Sod problem at $t_{\text{final}} = 0.2$.

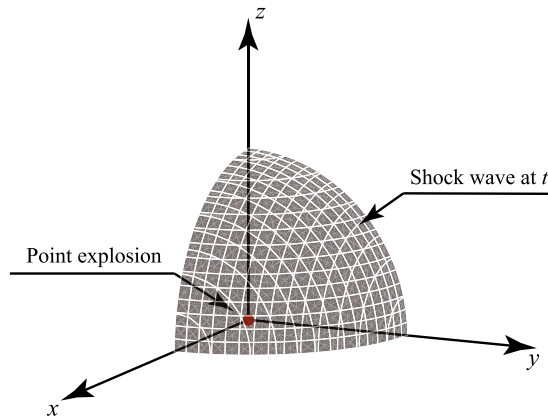


Fig. 18. Initial state and shock wave at physical time t of Sedov point explosion.

The problem is calculated with both MMALE and ls-MMALE for contrast. The Euler step is conducted when maximum ratio of side lengths reaches 4 or the largest inclined angle satisfies $\cos\theta \leq 0.7$. The quality criterion for determining the distorted cells is set to be $Q_l < 0.999$ and the objective grid quality criterion is set to be $Q_{\min} > 0.999$. The prescribed maximum number of iterations N_{\max} in each Euler step is 20. The density contour at different physical time is shown in Fig. 19 in which the propagation of the shock wave can be seen clearly and the density discontinuity surface is well maintained during the whole process. The radial density distribution at the final time of the ls-MMALE and the MMALE are compared with the analytical solution as illustrated in Fig. 20(a). As the distorted cells near the material interface are rezoned into nearly regular cells with the criterion $Q_{\min} > 0.999$, the numerical solutions obtained by the ls-MMALE and MMALE are completely consistent with each other and basically consistent with the analytical solution, which shows the correctness of the LSSM.

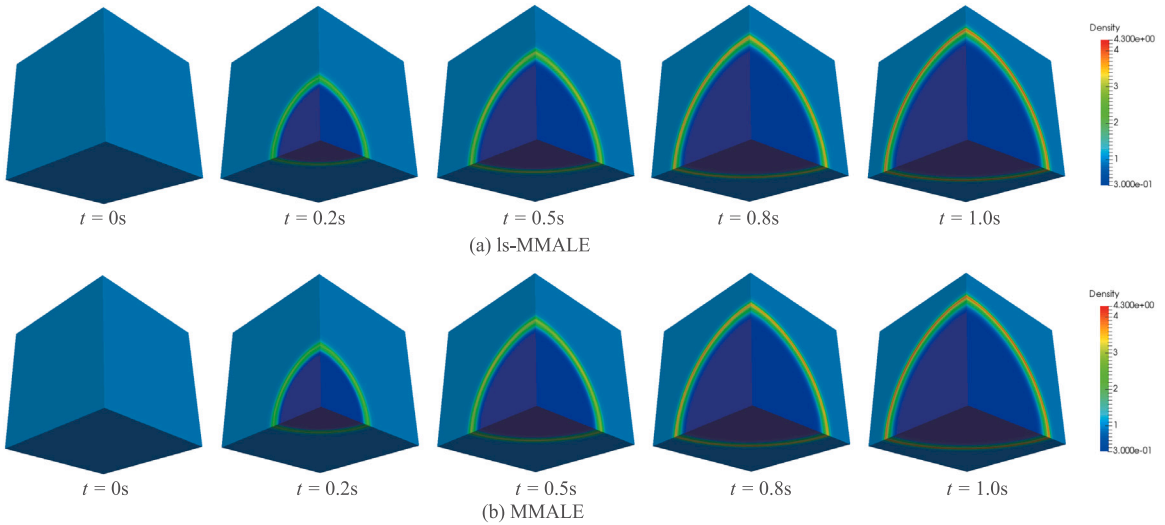


Fig. 19. Density contour at different time ($t = 0, 0.2, 0.5, 0.8, 1.0$) obtained by ls-MMALE and MMALE.

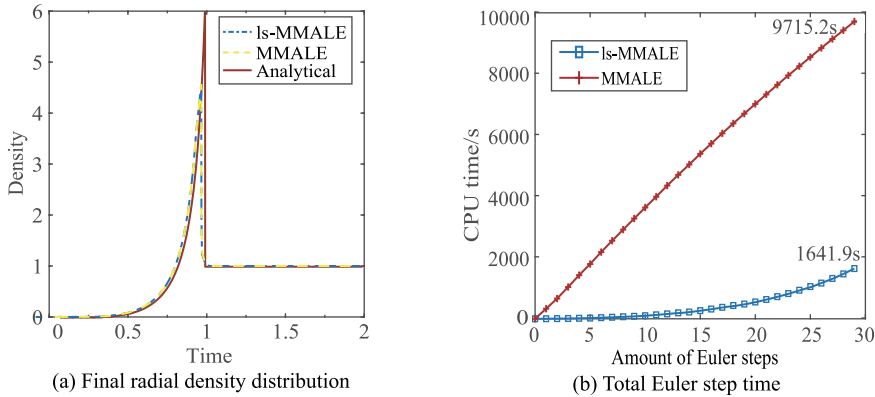


Fig. 20. Comparison of the density distribution and CPU time of ls-MMALE and MMALE: (a) final radial density distribution curves of ls-MMALE, MMALE and analytical; (b) comparison of CPU time with the amount of Euler steps in ls-MMALE and MMALE.

The CPU time versus the amount of Euler steps calculated with ls-MMALE and MMALE is shown in Fig. 20(b). The CPU time of each Euler step increases with the shock wave propagation. At last the shock front propagates to nearly the boundary of the computational domain but the CPU time for a Euler step with ls-MMALE is still much less than that with MMALE, as localized subdomains are automatically determined around the shock front face in which distorted cells exist. The total CPU time in Euler phase calculated with ls-MMALE is 0.169 times of that with MMALE, as shown in Table 1. In this and the subsequent problems, the CPU time is measured on a computer with an Intel(R) Xeon(R) Gold 6248R CPU (3.00 GHz) and 64 bit Linux operating system.

Table 1
The CPU time in Euler phase and amount of Euler steps.

Simulation method	CPU time/s	Amount of Euler steps
MMALE	9715.2	29
ls-MMALE	1641.9	29

7.4. Moving projectiles in fluid

In simulation of problems with structural fragmentation, small fragments may be generated and move in the fluid, making the computational grid distorted and global remapping occur frequently. Therefore the problems of moving projectiles in the fluid domain are considered here to show the great improvement of ls-ALEPM in computational efficiency.

Firstly a dimensionless analysis of one projectile rotating in the fluid domain $[-\frac{L}{2}, \frac{L}{2}] \times [-3.5, 3.5] \times [0, 0.025]$ is conducted as illustrated in Fig. 21, where the length of the fluid L is n ($n = 4, 5, 6, 7, 8$) times of the projectile length and is used for comparison

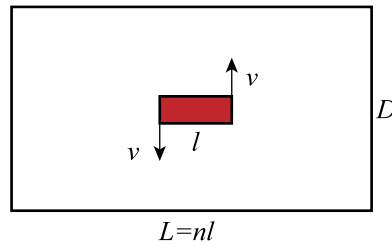


Fig. 21. A rotating projectile in the fluid domain.

of computational efficiency with different domain sizes. The fluid has a density of 1 and an internal energy per cell volume of 2.5. The projectile has a density of 1.0×10^6 with the Young's modulus 1.0×10^6 and the Poisson's ratio 0.3, which is initially located at $[-0.5, 0.5] \times [-0.1, 0.1] \times [0, 0.025]$ and rotates with an initial angular velocity of 2. The Euler step is conducted when maximum ratio of side lengths reaches 2 or the largest inclined angle satisfies $\cos\theta \leq 0.85$. The quality criterion used to recognize the distorted cells is set to be $Q_i < 0.999$ while the objective grid quality criterion is set to be $Q_{\min} > 0.9999$. The prescribed maximum number of iterations $N_{\max} = 20$ and the computation continues until t reaches 0.5.

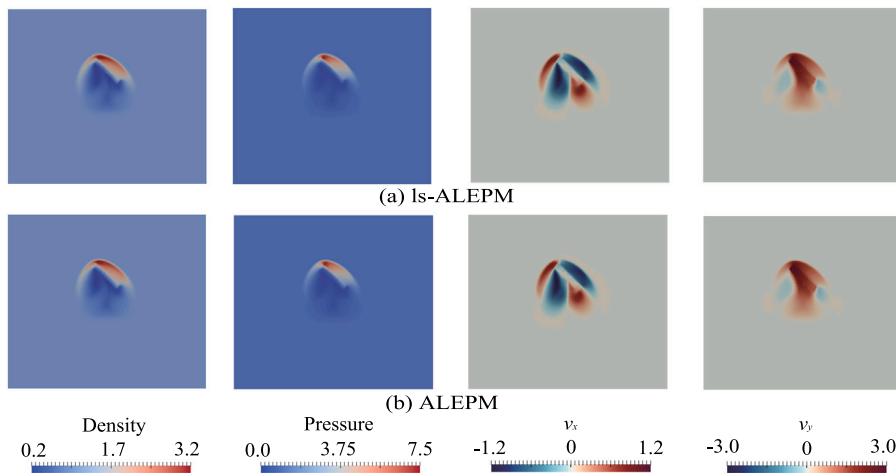


Fig. 22. Density, pressure, velocity in x - and y - direction in fluid domain influenced by the movement of two rotating projectiles.

The ls-ALEPM successfully identifies the distorted areas during the computation process and expanded the localized subdomains with the movement of the projectile. During the whole Euler phase, the transfinite interpolation method is not triggered. The contours of the density, speed and pressure at the same physical time calculated by the ls-ALEPM are compared with that calculated by the ALEPM as shown in Fig. 22. The results are almost the same and shows the correctness of ls-ALEPM. The little difference is because some areas are rezoned with transmission of physical quantities while others still remain unchanged.

Table 2

Comparison of CPU time in Euler phase.

Simulation method	ALEPM	ls-ALEPM
CPU time/s	3865.26	212.22

The comparison of the CPU time with different sizes of the computational domain is shown in Fig. 23. As the distorted areas are not changed with the domain size in ls-ALEPM, the CPU time of Euler phase remain unchanged. The total CPU time of ls-ALEPM grows slowly with the domain sizes as the Lagrangian phase is related to the amount of cells. However the CPU time of Euler step grows rapidly with the domain size in the ALEPM as all cells are intersected with the old grid. When the length ratio $n = 8$, the CPU time for the Euler phase with ls-ALEPM is nearly 0.078 times of that with ALEPM as illustrated in Table 2, which shows great improvement in computational efficiency.

Then the problem of nine projectiles moving in the fluid domain $[0, 300] \times [0, 100] \times [0, 60]$ is studied to test the ability of ls-ALEPM in dealing with multiple distorted areas. Three projectiles translate along the x , y , and z axes respectively with the initial velocity of 0.1 and three other projectiles rotates around the x , y , and z axes respectively with the initial angular velocity of 3. The other three projectiles move along and rotate around the x , y , and z axis with the initial velocity of 0.1 and initial angular velocity 3 respectively. The location of the projectiles at physical time 0.5 is shown in Fig. 24 in which the result of ls-ALEPM is nearly the same with that of ALEPM but with significantly higher computational efficiency as shown in Table 3.

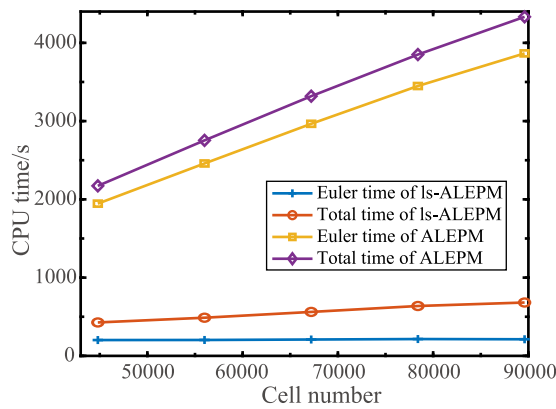


Fig. 23. The CPU time of Euler step and whole computation process with the increase of cell number in ls-ALEPM and ALEPM.

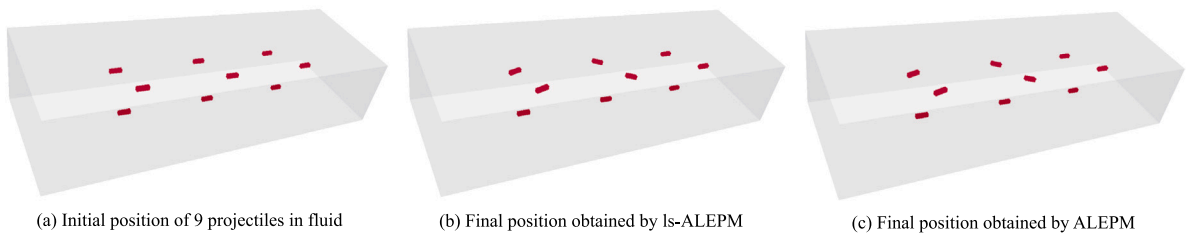


Fig. 24. Nine projectiles moving in the fluid.

Table 3
Comparison of CPU time in Euler phase with ALEPM and ls-ALEPM.

Simulation method	ALEPM	ls-ALEPM
CPU time/s	119 600	5846

7.5. The bending of a flexible plate induced by shock wave

Experimental and numerical studies of elastic bodies under hydrodynamic forces have been widely conducted [79–81]. The FSI problem studied here is a bending flexible plate induced by shock wave which serves as a validation case to show the performance of ALEPM in dealing with the large deformation problems. This problem is treated as a plain strain problem as illustrated in Fig. 25 and the dimensionless parameters of the solid and fluid are given as: Young’s modulus $E = 60\,000$, Poisson’s ratio $\nu = 0.45$, density of the solid $\rho_s = 1000$, the height $l = 1$ and length $d = 0.05$ of the plate, the internal energy per unit volume for the fluid $E_0 = 0.25$, the velocity for the inflow $U = 1$, the height for the fluid domain $D = 2$, the fluid density $\rho_f = 1$ for the first case and $\rho_f = 2$ for the second case. The computational domain is set to be $[0, 15] \times [0, 2] \times [0, 0.01]$. The symmetric boundaries at $y = 0$ and $y = 2$ are set while the boundaries at $x = 0$ and $x = 15$ are inflow and outflow boundaries respectively. The x -direction displacement of the gauge point in the upper-left corner of the plate is recorded to compare the history curves of the displacement in the x -direction and marked as red triangles in Fig. 25.

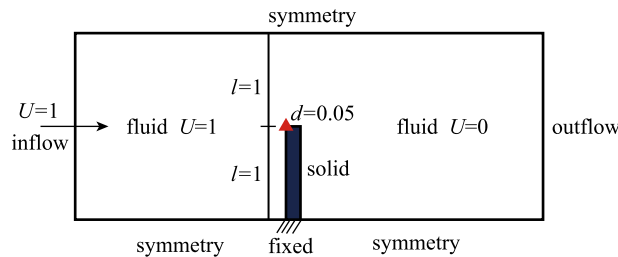


Fig. 25. Problem description for the flexible plate induced by shock wave.

The decoupled and original stress updating schemes of ALEPM are adopted for the computation and compared with the results of the immersed boundary-material point method (IBMPM) [59] and ANSYS AUTODYN (V19.2). The IBMPM adopts the MPM for the solid and the MUSCL interpolation FVM for the fluid, which handles shock-structure interaction well with the Lagrangian

continuous-forcing immersed boundary method and is validated by benchmarks and experimental results [59]. In both ALEPM and IBMPM, the fluid domain is discretized with the cell length 0.01 in all directions and the solid is discretized into particles with spacing 0.005 for contrast. The Lagrange solver (FEM) is adopted for the solid and Euler-FCT (FVM) solver is adopted for the fluid in ANSYS AUTODYN with the fully coupled Euler/Lagrange interaction. The fluid domain is discretized with the same cell length 0.01 and the solid is discretized by elements with spacing 0.0125. Then the fluid cell length of 0.004 and element length of 0.005 are adopted for the AUTODYN with mesh refinement (AUTODYN-r) to serve as a precise solution for contrast.

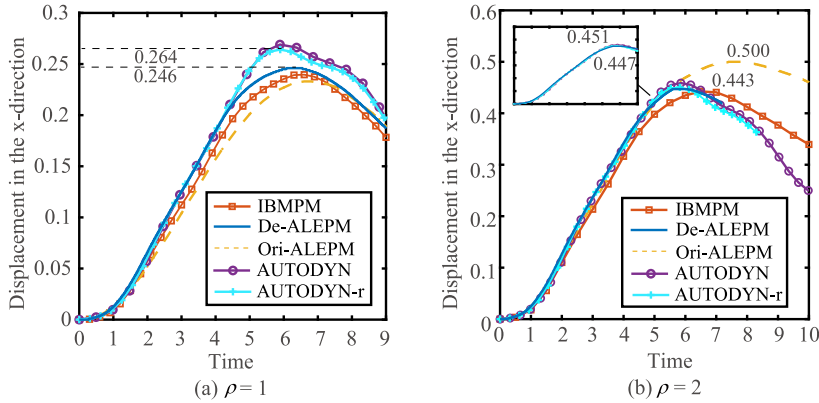


Fig. 26. Displacement of the gauge point in the x -direction obtained by different stress updating schemes in ls-ALEPM, IBMPM and AUTODYN.

Fig. 26 shows the displacement histories of the gauge point in the x -direction obtained with different methods and inflow densities. The displacement curves obtained by AUTODYN and AUTODYN with mesh refinement are basically consistent, which shows the size of discretization satisfies the accuracy requirement. The maximum magnitude of the displacement in the x -direction and the corresponding physical time simulated by different methods are shown in Table 4. The maximum displacement and the corresponding time simulated by the decoupled stress updating scheme of ALEPM are the closest to the results of AUTODYN in both cases. With the increase of the fluid density, the plate experiences larger deformation and the ratio of deflection to thickness reaches 9.02 from 5.28. Meanwhile the error of corresponding time with the original stress updating scheme and IBMPM reaches 29.13% and 16.55% when the fluid density $\rho_f = 2$, which are larger compared with the results of the presented method.

Table 4

Comparison of maximum displacements in the x -direction and time for the maximums with different methods.

Simulation method	Fluid density $\rho_f = 1$		Fluid density $\rho_f = 2$	
	Maximum displacement	Corresponding time	Maximum displacement	Corresponding time
Decoupled stress updating scheme	0.246/6.82%	6.080/3.77%	0.447/0.89%	5.590/2.32%
Original stress updating scheme	0.233/11.74%	6.520/11.28%	0.500/10.86%	7.390/29.13%
IBMPM	0.240/9.09%	6.470/10.43%	0.443/1.77%	6.670/16.55%
AUTODYN	0.269/1.89%	5.949/1.54%	0.458/1.55%	5.821/1.71%
AUTODYN with mesh refinement	0.264	5.859	0.451	5.723

The pressure contours at physical time $T = 4$ are shown in Fig. 27 in which the pressure distribution is roughly the same for decoupled stress updating scheme of ALEPM, IBMPM and AUTODYN. With the Riemann solver for the fluid, the pressure contour simulated by the IBMPM is closer to the results of AUTODYN-r compared with the presented ALEPM. The original stress updating scheme updates the solid stress with mixed velocity field and thereby applies inaccurate FSI forces on the fluid. High pressure of the fluid behind the plate is generated and the pressure contour is influenced by the nonphysical shock wave as shown in Fig. 27(b), which shows the effects of different stress updating methods on the FSI coupling and fluid field.

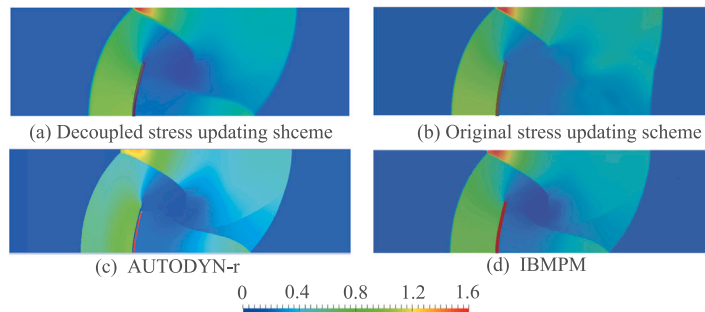


Fig. 27. Pressure contours in fluid domain at time $T = 4$ obtained by different stress updating schemes in ls-ALEPM, IBMPM and AUTODYN-r.

7.6. Fragmentation of a cylinder shell induced by blast

This section simulates the dynamic fracture of a 1045 steel cylindrical shell under blast loads with the decoupled and original stress updating scheme. Tang [82] carried out the explosion experiments and Yang et al. [83] simulated this problem with both the explosive and steel shell discretized by MPM particles.

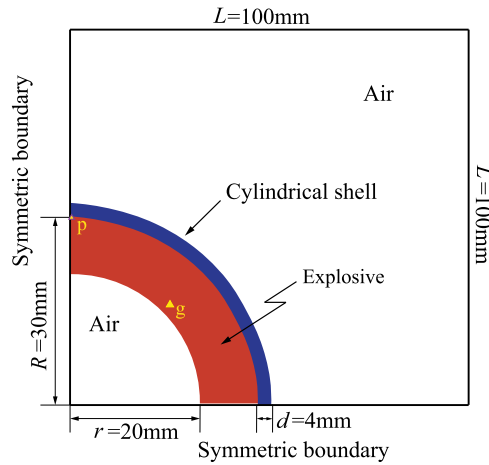


Fig. 28. Simulation set-up of cylindrical shell fragmentation driven by detonation.

As shown in Fig. 28, this problem is treated as a plain strain problem and 1/4 of the cylindrical shell is simulated due to symmetry. The computational domain is set to be $[0, 100 \text{ mm}] \times [0, 100 \text{ mm}] \times [0, 0.5 \text{ mm}]$ with the cell length 0.5 mm in all directions. Symmetric boundaries at $x = 0$ and $y = 0$ are set while the boundaries at $x = 100 \text{ mm}$ and $y = 100 \text{ mm}$ are applied with air pressure. The ideal gas is adopted for the air whose density and internal energy per unit volume are $\rho_{\text{air}} = 1.2 \times 10^{-6} \text{ g/mm}^3$ and $E_0 = 0.266772 \text{ mJ/mm}^3$ respectively. The explosive is RHT-901 with a density of $\rho = 1.684 \times 10^{-3} \text{ g/mm}^3$ and an internal energy per cell volume of $E_0 = 6853.9 \text{ mJ/mm}^3$. The inner radius of the explosive is $r = 20 \text{ mm}$ and the outer radius is $R = 30 \text{ mm}$. A gauge point g marked as triangles in Fig. 28 is set at $r_1 = 22$ to record the pressure history of the fluid. The particle p initially located at $(0, 30, 0.125)$ is also recorded the pressure history of the stress. The JWL equation of state is adopted for the explosive with the parameters taken from the article [84] as $A = 524.2 \text{ GPa}$, $B = 0.0321 \text{ GPa}$, $R_1 = 4.15$, $R_2 = 0.95$, $\omega = 0.3$.

The cylindrical shell has an inner radius R of 30 mm and the thickness h is of 4 mm which is discretized by particles with spacing 0.25 mm. The 1045 steel has a density of 7800 kg/m^3 , Young's modulus of 210 GPa and Poisson's ratio of 0.3 according to the literature [85] and is described by the simplified Johnson-Cook model as

$$\sigma_y = \left(A + B \bar{\epsilon}_p^n \right) \left(1 + C \ln \bar{\epsilon}_p^* \right) \tag{59}$$

where $A = 5.07 \times 10^5 \text{ MPa}$, $B = 3.2 \times 10^3 \text{ MPa}$, $n = 0.28$, $C = 0.064$ [85]. Gurson model [86] incorporated with a TEPLA-F failure condition is employed to model the microscopic defects with randomly distributed initial void fraction. The fracture strain of the shell is measured to be $\epsilon_p^f = 0.43$ in Tang's [82] experiment and the other parameters are shown in Table 5 where f_{0e} denotes the mean of the initial void fraction, f_{0s} denotes the variance of the initial void fraction, q_1 , q_2 , f_f , f_c , f_N , ϵ_N , and s_N are other parameters of Gurson model. The Mie-Gruneisen EOS is adopted to update the volumetric stress of steel shell with parameters $c_0 = 3570 \text{ mm/ms}$, $s_1 = 1.92$ and $\gamma_0 = 1.8$.

Table 5
The constants of Gurson model for 1045 steel [87].

q_1	q_2	f_{0e}	f_{0s}	f_f	f_c	f_N	ϵ_N	s_N	ϵ_p^f
1.5	1	0.005	0.0003	0.0021	0.2109	0.001	0.04	0.01	0.43

The pressure contours of the fluid and failure contours of the cylindrical shell obtained by the decoupled and original stress updating scheme from $10 \mu\text{s}$ to $60 \mu\text{s}$ are shown in Figs. 29 and 30. The particles after failure are colored in red while those before failure are in blue. At the beginning of the simulation $t = 0$, the explosive is detonated and the generated shock wave will drive the cylindrical shell to expand. The shear instability and dynamic failure occurs at the inner side of the shell where the material is compressed by the explosive. Then the outer side of the shell are in tension along the circumferential direction and tensile fracture is generated. The mixed tensile-shear fracture grows up and forms the complete red cracks along the thickness. After a period of time, a shock wave which reflects from the symmetry boundary catches up with and drives the shell fragments to accelerate. Both the decoupled and original stress updating scheme reproduce the whole process with the stationary flow, shock wave and reflection wave captured clearly.

The pressure history curves at spatial point g of $r_1 = 22$ and particle p at $(0, 30, 0.125)$ are plotted in Fig. 31 which shows the difference between the two schemes. With the influence of fluid velocity, the pressure and stress calculated by the original

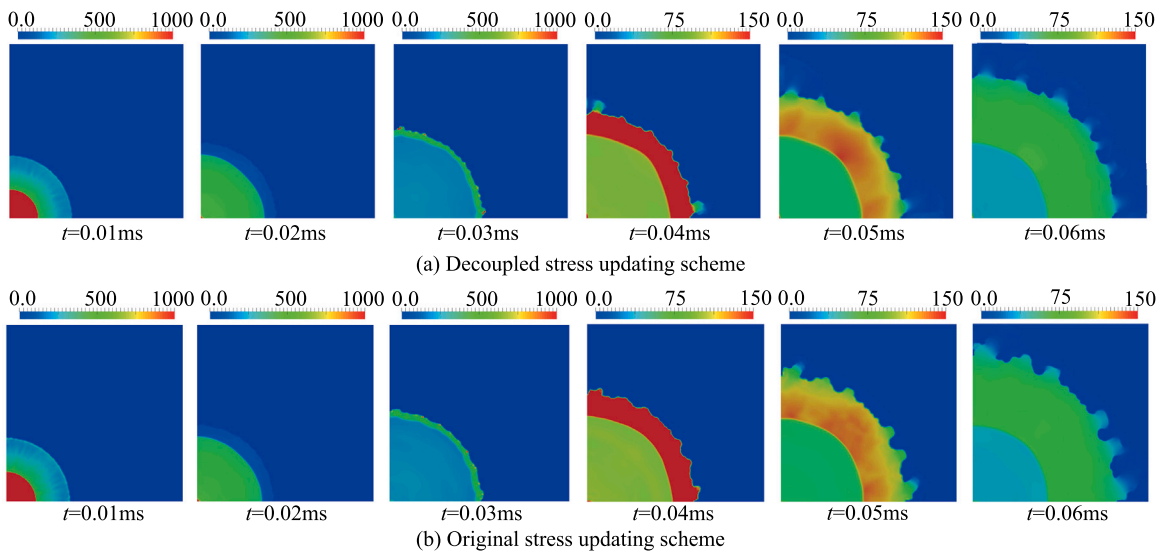


Fig. 29. Pressure contours in fluid domain from 0 μ s to 60 μ s obtained by different stress updating schemes.

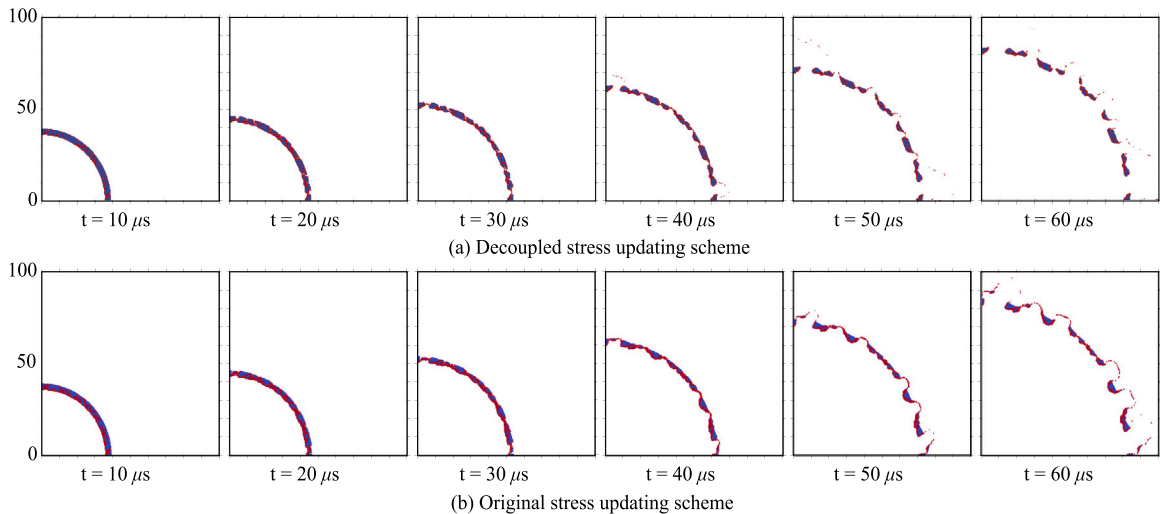


Fig. 30. Cylindrical shell failure contour from 0 μ s to 60 μ s obtain by different stress updating schemes.

stress updating scheme experiences severe oscillation and are overestimated compared with that by the decoupled stress updating scheme. The first peak pressure of the two methods are nearly the same while the second peak pressure of reflection calculated by the decoupled stress updating scheme is smaller than that by the original stress updating scheme as it calculates the solid stress accurately by eliminating the influence of the fluid.

Moreover, the results of the two schemes on solid fragmentation are not the same. Particles at the inner side of the shell fail at the very beginning and form smaller fragments after severe fracture with the original stress updating scheme. The physical time for the first crack calculated by the decoupled stress updating scheme is 8.3 μ s and is closer to 8.8 μ s of the experiment [82] compared with 8.0 μ s by the original stress updating scheme

The complete fragments of the cylinder is illustrated in Fig. 32 in which the decoupled stress updating scheme shows more reasonable and symmetrical failure in the circumferential direction. The midline width and thickness of main fragments calculated with the schemes are summarized in the Table 6 together with the results of the experiment from Tang [82]. It can be observed that the original stress updating scheme generates much smaller fragments compared with the experiment while the decoupled stress updating scheme obtains more accurate solid strain and stress as well as the sizes of fragments.

7.7. Structural damage of open-frame building under explosion

Next, the damage of an open-frame building under explosion is studied with the decoupled and original stress updating scheme of ls-ALEPM. The explosion experiments as shown in Fig. 33(a) was conducted by Woodson and Baylot [88]. Baylot and Bevins [7]

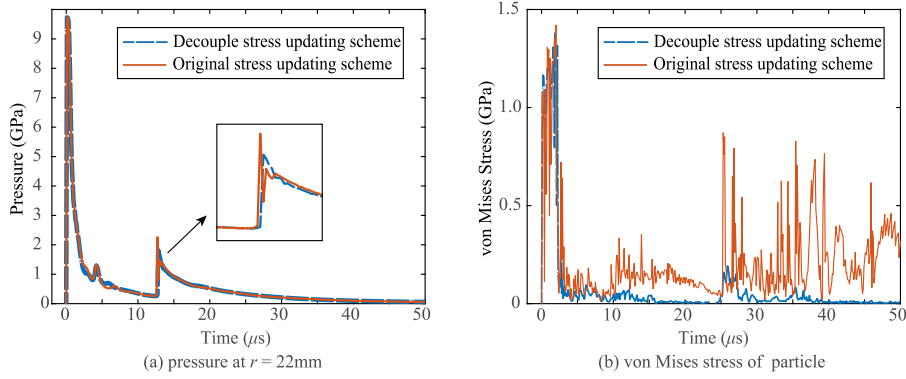


Fig. 31. Pressure histories of gauge g and particle p obtained by different stress updating schemes.

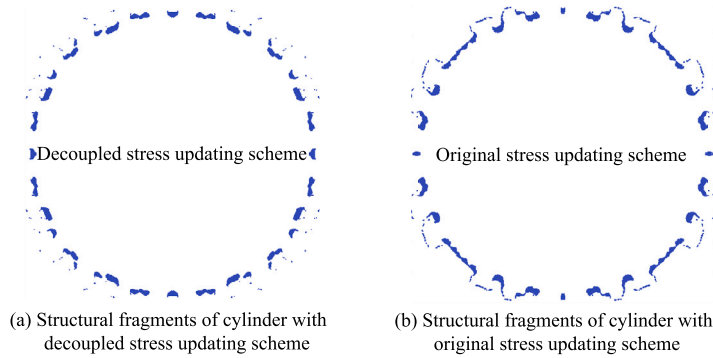


Fig. 32. Structural fragments at $t = 60 \mu s$ obtained by different stress updating schemes.

Table 6
Statistics of fragments' midline width and thickness at the end of simulation (Unit: mm).

Simulation method	Midline width/Thickness of main fragments						Average width/thickness	
The original stress updating scheme	Width	3.302	6.990	2.346	7.315	5.593	4.497	5.872/3.137 25.3%/4.94%
		7.858	5.738	6.063	11.300	3.587		
	Thickness	2.840	4.059	1.850	4.502	2.926	2.440	
		2.363	2.799	3.568	4.754	2.407		
The decoupled stress updating scheme	Width	5.876	12.064	9.339	4.046	3.353	10.925	7.799/3.264 0.78%/1.09%
		4.862	8.612	12.246	6.665			
	Thickness	3.268	3.364	3.753	2.376	2.376	3.678	
		2.760	3.683	3.161	3.333			
Experiment [82]	/						7.86/3.3	

studied this problem numerically using CTH code for blast loads and DYNA3D for structural damage. Due to symmetry, a 1/2 model is simulated here.

The size of the entire computational domain is $L = 3.1 \text{ m}$, $D = 1.7 \text{ m}$ and $H = 2.2 \text{ m}$. The hemispherical C4 explosive placed at $h = 0.305 \text{ m}$ from the ground has a mass of 7.1 kg whose equivalent TNT based on the same impulse [7] is of 8.449 kg . Due to symmetry, a 1/8 spherical TNT explosive with the mass of 2.11225 kg is used here which has a density of $1.63 \times 10^{-3} \text{ g/mm}^3$ and is described by JWL EOS with parameters as $A = 371.2 \text{ GPa}$, $B = 3.23 \text{ GPa}$, $R_1 = 4.15$, $R_2 = 0.95$, $w = 0.3$. The horizontal distance from the open-frame building to the explosive is 1.07 m . The open-frame building is a reinforced concrete structure and made up of two floors and four columns whose mechanical behavior of concrete is described by HJC model [7] as shown in Table 7. The parameters are the same as the experimental setting.

The mechanical behavior of the rebars is described by the linear strengthening plastic model with relative parameters density $\rho = 7.5 \times 10^{-3} \text{ g/mm}^3$, Young's modulus $E = 200 \text{ GPa}$ and Poisson's ratio $\nu = 0.3$. Three kinds of rebars are adopted for different parts of the building in the experiment whose yield strength, ultimate strength, the geometry size and the distribution are all from the experiment as shown in Table 8.

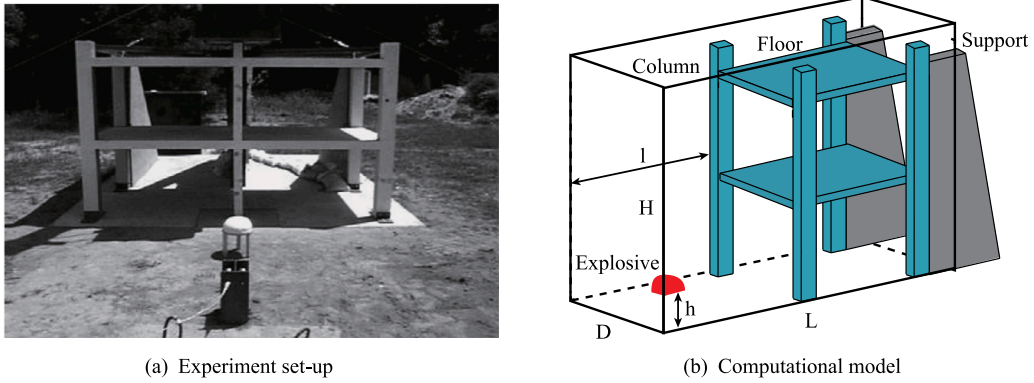


Fig. 33. Experiment set-up [88] and computational model of open-frame building under explosion.

Table 7
The parameters of HJC material model.

A	B	n	C	f'_c /MPa	S_{max}	T/MPa	D_1	D_2	$\epsilon_{f \min}$
0.79	1.60	0.61	0.007	42	7.0	4.1	0.04	1.0	0.001
p_{crush} /MPa	μ_{crush}	p_{lock} /GPa	μ_{lock}	K_1 /GPa	K_2 /GPa	K_3 /GPa			
12	0.001	0.8	0.10	85	-171	208			

Table 8
Geometry size and properties of reinforcement.[7]

Reinforcement	Area (mm ²)	Yield stress(MPa)	Ultimate Strength
W0.5	3.22	441	513
D1	6.45	399	610
D5	32.2	449	513

Typical contours of fluid pressure and building damage at different time are shown in Fig. 34 in which the explosive explosion generates a spherical shock wave and interacts with the lower center column to generate a high-pressure reflection wave. When impacted by the explosion wave at around $t = 0.6$ ms, the front of the center column is under overpressure, and then the back of the center column is under tensile waves due to the reflection of stress waves. The volume fraction contour of the fluid on the surface of $z = 0.4$ m and the pressure contour of the building are shown in Fig. 34 in which the explosive expands outward driven by the high-pressure waves and flows around the center column.

Throughout the load, the center column experiences large deformation and then rebounds with multiple vibrations. In this section, the computation continues until the first vibration process is finished to record the maximum displacement of the center column. Compared with the 9.8 mm (error percentage 16.92%) calculated by the original stress updating scheme, the maximum displacement 8.8 mm (error percentage 4.75%) calculated by the decoupled stress updating scheme is closer to the result 8.382 mm in literature [88].

As shown in Figs. 35(c) and 35(d), the decoupled stress updating scheme finally forms a damage crack along the center of the concrete, which is consistent with the experiment shown in Figs. 35(a) and 35(b). The original stress updating scheme gives larger stress due to the influence of the fluid velocity and thus crack appears and propagates at the height where blast wave first interacts with the column as illustrated in Fig. 35(e). Both the two methods successfully simulates the severe damage at the top and bottom of the lower center column, which is observed in the experiment and caused by strong shear. The concrete with $damg = 1$ in Figs. 35(c), 35(d), 35(e) and 35(f) is totally damaged while the rebars are not fractured, reproducing the experimental phenomena that the center column experienced severe destruction but without collapse. The non-physical failure of a thin layer of particles on the back of the center column appears when calculated with the original stress updating scheme, as illustrated in Fig. 35(f). Located at the FSI interface cells, the particles are damaged by the overestimated stress. By comparing Figs. 35(c), 35(d) and Figs. 35(e), 35(f), the decoupled stress updating scheme is in better agreement with the experiment and the stress overestimation is eliminated.

The problem is simulated by both ls-ALEPM and ALEPM to compare the CPU time and amount of Euler steps as shown in Table 9. The Euler step is conducted when maximum ratio of side lengths reaches 2 or the largest inclined angle satisfies $\cos\theta \leq 0.8$. The quality criterion used to recognize the distorted cells is set to be $Q_l < 0.99$ and the objective grid quality criterion is set to be $Q_{\min} > 0.997$ with $N_{\max} = 20$. Although ls-ALEPM triggers more Euler steps, the CPU time of each Euler step is greatly reduced and the total CPU time is about 0.1485 times of the ALEPM. During the computation, the shock wave propagation and reflection as well as the interaction with the columns and floors make the remeshing frequently performed. Although almost all grid cells are influenced by the fluid flow at the end of the simulation, ls-ALEPM still achieves a good acceleration effect and has not failed.

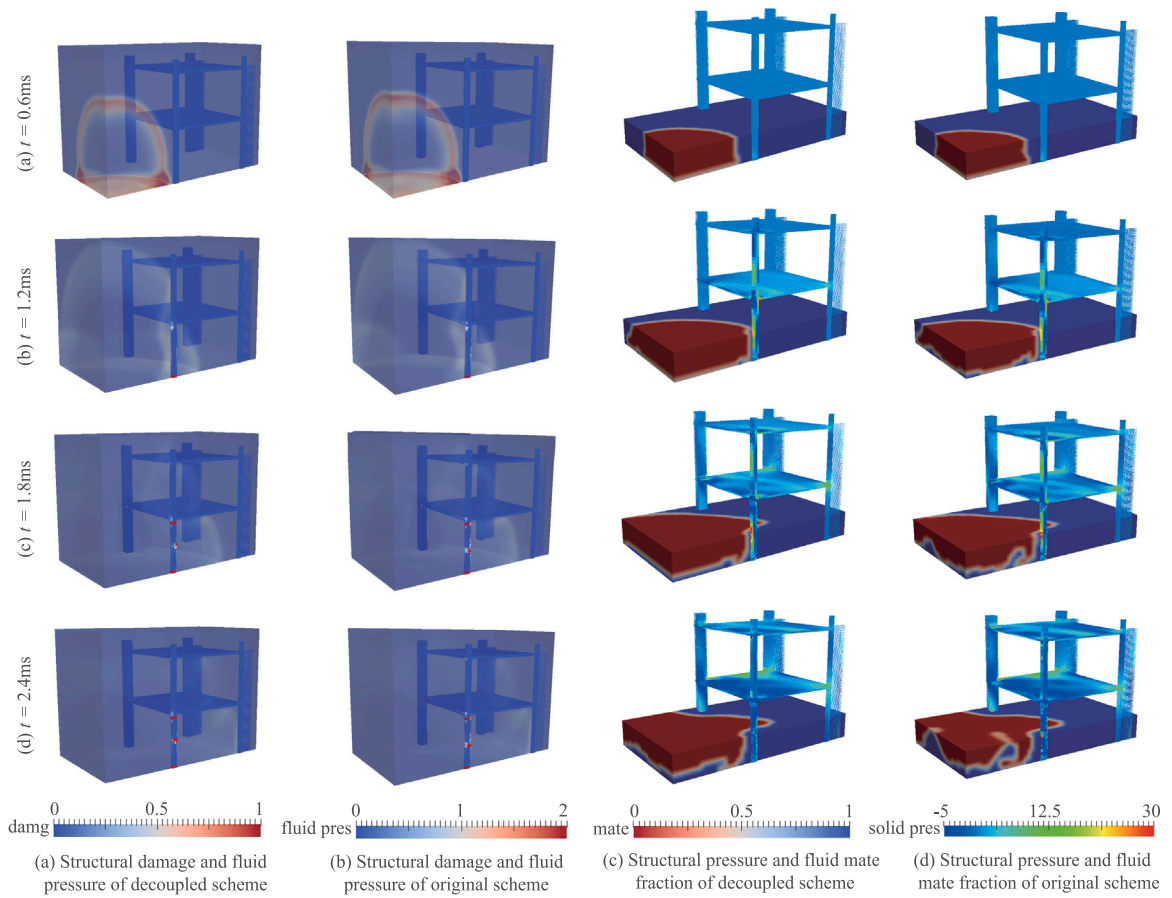


Fig. 34. Damage, pressure and material fraction contour at different time ($t = 0.6$ ms, 1.2 ms, 1.8 ms, 2.4 ms) of open-frame building and fluid domain.

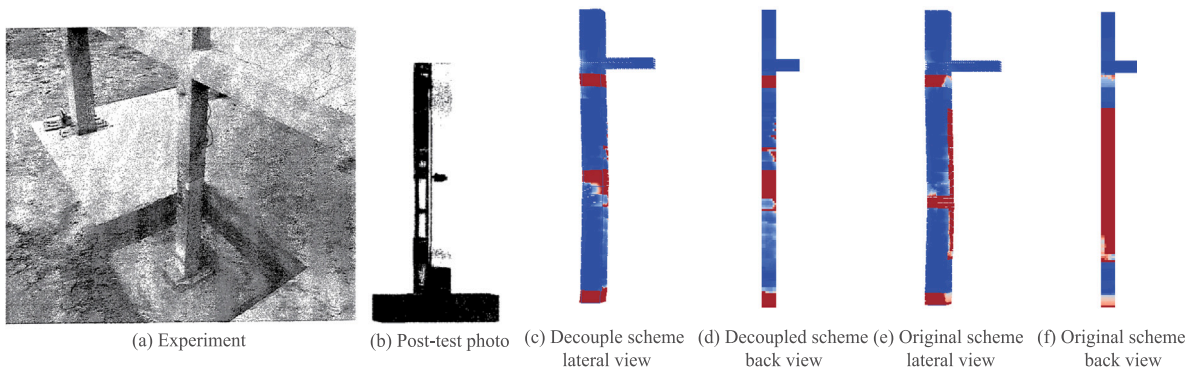


Fig. 35. Comparison of damage in experiment and numerical simulations with the decoupled stress updating scheme and the original stress updating scheme in ls-ALEPM.

Table 9

CPU time in Euler phase and amount of Euler steps.

Simulation method	CPU time/s	Amount of Euler steps
ALEPM	332614.89	101
ls-ALEPM	49400.19	104

7.8. Implosion of a below-grade concrete garage

The implosion of a 3-story building is studied with both ls-ALEPM and ALEPM. Tegeler et al. [89] developed a finite element model for a below-grade concrete garage and studied it with the ABAQUS/Explicit code. The size of the garage is $L = 40$ m, $D = 40$ m, and $H = 10.8$ m as illustrated in Fig. 36. The nine supporting square pillars of the garage all have the cross section of $0.8\text{ m} \times 0.8\text{ m}$ with spacing 10 m and the thickness of the floor slabs are all 0.42 m . The passages to other floors of the garage are also considered in the end-wall of each floor with the size of $6\text{ m} \times 2.5\text{ m} \times 0.42\text{ m}$. The 45.4 kg TNT with a vertical standoff of 1 m from the second floor slab is adopted for the implosion and the material perimeters are the same as Section 7.7. The concrete garage has a density of $2.643 \times 10^{-3}\text{ g/mm}^3$, the Young’s modulus of 31.027 GPa and the Poisson’s ratio of 0.2 with the compressive initial yield stress 13.0 MPa , the compressive ultimate stress 24.1 MPa and the tensile fracture stress 2.9 MPa , which are all taken from the literature [89]. The Euler step is conducted when maximum ratio of side lengths reaches 4 or the largest inclined angle satisfies $\cos\theta \leq 0.7$. The quality criterion used to recognize the distorted cells is set to be $Q_i < 0.99$ and the objective grid quality criterion is set to be $Q_{\min} > 0.997$ with $N_{\max} = 20$. The results obtained by ls-ALEPM and ALEPM are shown in Fig. 37 in which both shock waves reach the back of the two nearest columns at physical time 4 ms and are consistent with the simulation of ABAQUS ConWep. The shape and size of the failure area simulated by ls-ALEPM and ALEPM are also the same and similar with the finite element model.

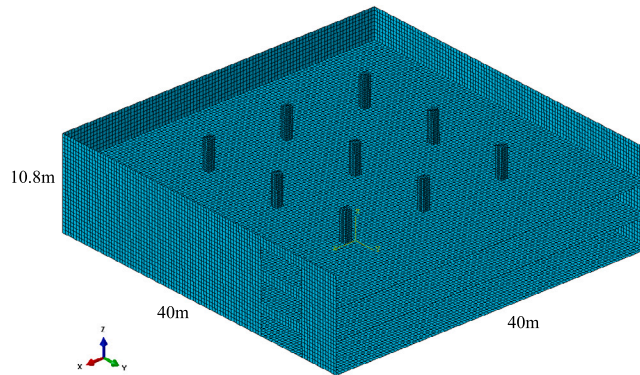


Fig. 36. Pseudo-experiment simulation model of garage implosion [89].

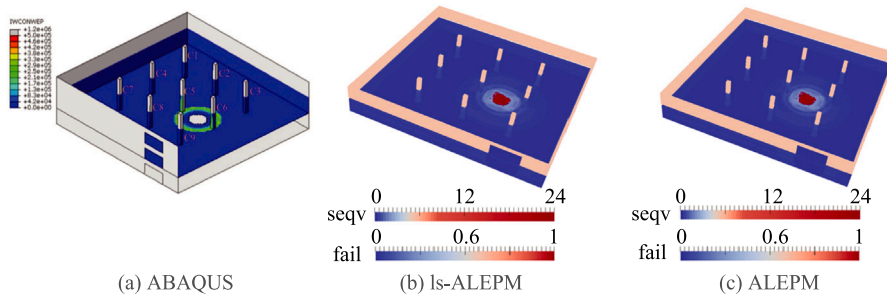


Fig. 37. Comparison of structural failure and loads of ABAQUS, ls-ALEPM and ALEPM: (a) the propagation of the incident wave pressure loads(CONWEP) and structural failure(removed) on surface at 4ms [89]; (b) the von Mises stress and structural failure (in red) on surface at 4 ms with ls-ALEPM; (c) the von Mises stress and structural failure(in red) on surface at 4 ms with ALEPM;.

The CPU time calculated with ls-ALEPM and ALEPM are shown in Table 10. As the size of the whole computational domain is very huge and the structural damage is only concentrated in a localized area, the improvement of efficiency is very significant and the ratio of CPU time is $1: 15.575$.

Table 10
Comparison of CPU time in Euler phase in ALEPM and ls-ALEPM.

Simulation method	ALEPM	ls-ALEPM
CPU time/s	1.1298×10^5	2.408×10^3

8. Conclusions

A localized subdomain smoothing MMALE particle method (ls-ALEPM) is proposed in this paper for efficient and accurate simulations of large scale FSI problems. In order to avoid the spurious strain induced by the mixed FSI velocity field, a decoupled stress updating scheme is proposed to update the stress of solid particles by introducing a virtual velocity field in the vicinity of FSI interface. The strains of solid particles located at the interface cells are updated with the solid velocity field and separated from fluid velocity. Therefore the accurate solid stress is obtained and stress oscillation caused by the mixed FSI velocity field is eliminated.

Theoretical analysis is conducted with the nodal velocities of mixed cells as well as the solid strain and stress and the reasons for pressure oscillation of fluid and overestimated stress of solid are also derived.

The novel ls-ALEPM is also combined with the localized subdomain smoothing method (LSSM) for the Euler step, which is time-consuming with the intersection based remapping. The localized subdomain smoothing method (LSSM) is put forward to accelerate the remapping phase and only involves the distorted regions of computational grid. LSSM is composed of the distorted subdomain determination step and the combined mesh smoothing step. Each iteration step of the combined mesh smoothing step is composed of the modified GETMe and weighted average method while the transfinite interpolation method is adopted as a supplementary process. The ls-ALEPM takes the advantages of different methods and realize accurate and consistent rezoning and remapping.

Several benchmark numerical examples and practical engineering problems are simulated to verify the correctness and superiority of the ls-ALEPM. Comparing the effects of different methods, the smoothing benchmark of 3D distorted grid examines the effectiveness and correctness of LSSM. The Sedov point explosion problem tests the computational efficiency of ls-MMALE to deal with problems with shock wave propagation and large distorted areas. The moving projectiles in fluid examines the improvement of efficiency with ls-ALEPM and the fragmentation of a cylinder shell induced by blast examines the effectiveness and correctness of the decoupled stress updating scheme when simulating problems with the structure fragmentation. The structural damage of open-frame building under explosion shows the capability of ls-ALEPM in simulating problems with structural damage. The pseudo-experiment simulation of garage implosion shows high efficiency of ls-ALEPM in large-scale engineering problems. The results all fit well with the theoretical solution, the experimental data, indicating that ls-ALEPM is effective and efficient for solving multi-phase flow and FSI problems.

For future directions, as the piecewise linear shape function whose gradient is discontinuous on the cell boundary is employed in the standard MPM, cell crossing noise is generated and the accuracy of the solid stress is limited in the MMALE particle method. Improved MPM methods with high-order accuracy can be adopted in the MMALE particle method and enhance the accuracy of solid region and fluid–structure-interaction. Meanwhile the localized subdomain rezoning method accompanied with topology changes can also be considered in ls-ALEPM which can realize high efficiency with adaptive local mesh refinement. Further consideration should also be given to the water-entry and structural damage problems involving the cavitation with the proposed decoupled stress updating scheme, which are widely concerned and challenging FSI problems. Different cavitation models and algorithms as well as more precise and robust methods to reconstruct the multi-phase interface should be investigated, which can be introduced into the proposed method.

Declaration of competing interest

We declare that we have no financial and personal relationships with other people or organizations that can inappropriately influence our work, there is no professional or other personal interest of any nature or kind in any product, service and/or company that could be construed as influencing the position presented in, or the review of, the manuscript

Data availability

Data will be made available on request.

References

- [1] W. Liang, J. Zhao, H. Wu, K. Soga, Multiscale, multiphysics modeling of saturated granular materials in large deformation, *Comput. Methods Appl. Mech. Engrg.* 405 (2023) 115871.
- [2] Z. Wang, M. Soomro, C. Peng, L.F. Ayala, O.M. Ayala, Two pressure boundary conditions for multi-component multiphase flow simulations using the pseudo-potential lattice Boltzmann model, *Comput. & Fluids* 248 (2022) 105672.
- [3] G. Ma, H.H. Bui, Y. Lian, K.M. Tran, G.D. Nguyen, A five-phase approach, SPH framework and applications for predictions of seepage-induced internal erosion and failure in unsaturated/saturated porous media, *Comput. Methods Appl. Mech. Engrg.* 401 (2022) 115614.
- [4] A. Negara, A. Salama, S. Sun, Multiphase flow simulation with gravity effect in anisotropic porous media using multipoint flux approximation, *Comput. & Fluids* 114 (2015) 66–74.
- [5] Y.-X. Peng, A.-M. Zhang, F.-R. Ming, Numerical simulation of structural damage subjected to the near-field underwater explosion based on SPH and RKPM, *Ocean Eng.* 222 (2021) 108576.
- [6] M.A. Puso, J. Sanders, R. Settgast, B. Liu, An embedded mesh method in a multiple material ALE, *Comput. Methods Appl. Mech. Engrg.* 245–246 (2012) 273–289.
- [7] J.T. Baylot, T.L. Bevins, Effect of responding and failing structural components on the airblast pressures and loads on and inside of the structure, *Comput. Struct.* 85 (11–14) (2007) 891–910.
- [8] A. Franci, E. Onate, J. Maria Carbonell, M. Chiumenti, PFEM formulation for thermo-coupled FSI analysis. Application to nuclear core melt accident, *Comput. Methods Appl. Mech. Engrg.* 325 (2017) 711–732.
- [9] G. Li, J. Gao, P. Wen, Q. Zhao, J. Wang, J. Yan, A. Yamaji, A review on MPS method developments and applications in nuclear engineering, *Comput. Methods Appl. Mech. Engrg.* (ISSN: 0045-7825) 367 (2020) 113166.
- [10] W.-T. Liu, A.-M. Zhang, X.-H. Miao, F.-R. Ming, Y.-L. Liu, Investigation of hydrodynamics of water impact and tail slamming of high-speed water entry with a novel immersed boundary method, *J. Fluid Mech.* 958 (2023).
- [11] I. Hammani, S. Marrone, A. Colagrossi, G. Oger, D. Le Touze, Detailed study on the extension of the delta-SPH model to multi-phase flow, *Comput. Methods Appl. Mech. Engrg.* 368 (2020) 113189.
- [12] V.-T. Nguyen, D.-T. Vu, W.-G. Park, C.-M. Jung, Navier-Stokes solver for water entry bodies with moving Chimera grid method in 6DOF motions, *Comput. & Fluids* 140 (2016) 19–38.

- [13] Z. Ma, L. Qian, P. Martínez-Ferrer, D. Causon, C. Mingham, W. Bai, An overset mesh based multiphase flow solver for water entry problems, *Comput. & Fluids* 172 (2018) 689–705.
- [14] Z. Jia, J. Liu, S. Zhang, An effective integration of methods for second-order three-dimensional multi-material ALE method on unstructured hexahedral meshes using MOF interface reconstruction, *J. Comput. Phys.* 236 (2013) 513–562.
- [15] C. Hirt, A. Amsden, J. Cook, An arbitrary Lagrangian-Eulerian computing method for all flow speeds, *J. Comput. Phys.* 14 (3) (1974) 227–253.
- [16] X. Zheng, G. Karniadakis, A phase-field/ALE method for simulating fluid-structure interactions in two-phase flow, *Comput. Methods Appl. Mech. Engrg.* 309 (2016) 19–40.
- [17] G. Anjos, N. Mangiavacchi, J. Thome, An ALE-FE method for two-phase flows with dynamic boundaries, *Comput. Methods Appl. Mech. Engrg.* 362 (2020) 112820.
- [18] D.J. Benson, An efficient, accurate, simple ale method for nonlinear finite element programs, *Comput. Methods Appl. Mech. Engrg.* 72 (3) (1989) 305–350.
- [19] L. Pan, F. Zhao, K. Xu, High-order ALE gas-kinetic scheme with WENO reconstruction, *J. Comput. Phys.* 417 (2020) 109558.
- [20] Q. Li, G. qiang He, P. jin Liu, J. Li, Coupled simulation of fluid flow and propellant burning surface regression in a solid rocket motor, *Comput. & Fluids* 93 (2014) 146–152.
- [21] J.S. Peery, D.E. Carroll, Multi-Material ALE methods in unstructured grids, *Comput. Methods Appl. Mech. Engrg.* 187 (3–4) (2000) 591–619.
- [22] X. Chen, X. Zhang, An improved 2D MoF method by using high order derivatives, *J. Comput. Phys.* 349 (2017) 176–190.
- [23] H.T. Ahn, M. Shashkov, Multi-material interface reconstruction on generalized polyhedral meshes, *J. Comput. Phys.* 226 (2) (2007) 2096–2132.
- [24] F. Qing, Z. Jia, L. Liu, A cell-centered discontinuous Galerkin multi-material arbitrary Lagrangian-Eulerian method in axisymmetric geometry, *J. Comput. Phys.* 473 (2023) 111745.
- [25] M. Kucharik, R.V. Garimella, S.P. Schofield, M.J. Shashkov, A comparative study of interface reconstruction methods for multi-material ALE simulations, *J. Comput. Phys.* 229 (7) (2010) 2432–2452.
- [26] F. Qing, X. Yu, Z. Jia, A robust MoF method applicable to severely deformed polygonal mesh, *J. Comput. Phys.* 377 (2019) 162–182.
- [27] J. Velechovsky, E. Kikinzon, N. Ray, H. Rakotoarivelo, A. Herring, M. Kenamond, K. Lipnikov, M. Shashkov, R. Garimella, D. Shevitz, Multi-material swept face remapping on polyhedral meshes, *J. Comput. Phys.* 469 (2022) 111553.
- [28] V.P. Chiravalle, A. Barlow, N.R. Morgan, 3D Cell-centered hydrodynamics with subscale closure model and multi-material remap, *Comput. & Fluids* 207 (2020) 104592.
- [29] L. Margolin, M. Shashkov, Second-order sign-preserving conservative interpolation (remapping) on general grids, *J. Comput. Phys.* 184 (1) (2003) 266–298.
- [30] R. Garimella, M. Kucharik, M. Shashkov, An efficient linearity and bound preserving conservative interpolation (remapping) on polyhedral meshes, *Comput. & Fluids* 36 (2) (2007) 224–237.
- [31] D. Powell, T. Abel, An exact general remeshing scheme applied to physically conservative voxelization, *J. Comput. Phys.* 297 (2015) 340–356.
- [32] G. Blanchard, R. Loubère, High order accurate conservative remapping scheme on polygonal meshes using a posteriori MOOD limiting, *Comput. & Fluids* 136 (2016) 83–103.
- [33] X. Chen, X. Zhang, Z. Jia, A robust and efficient polyhedron subdivision and intersection algorithm for three-dimensional MMALE remapping, *J. Comput. Phys.* 338 (2017) 1–17.
- [34] Z. Jia, J. Liu, S. Zhang, An effective integration of methods for second-order three-dimensional multi-material ALE method on unstructured hexahedral meshes using MOF interface reconstruction, *J. Comput. Phys.* 236 (2013) 513–562.
- [35] M. Berndt, J. Breil, S. Galera, M. Kucharik, P.-H. Maire, M. Shashkov, Two-step hybrid conservative remapping for multimaterial arbitrary Lagrangian-Eulerian methods, *J. Comput. Phys.* 230 (17) (2011) 6664–6687.
- [36] H. Yang, P. Zhang, A hybrid subcell-remapping algorithm for staggered multi-material arbitrary Lagrangian-Eulerian methods, *Appl. Math. Mech.* 40 (2019) 1487–1508.
- [37] L. Xie, Z. Kang, H. Hong, Z. Qiu, B. Jiang, Local mesh deformation using a dual-restricted radial basis functions method, *Aerosp. Sci. Technol.* 130 (2022) 107940.
- [38] R. Durand, B. Pantoja-Rosero, V. Oliveira, A general mesh smoothing method for finite elements, *Finite Elem. Anal. Des.* 158 (2019) 17–30.
- [39] W. Bo, M. Shashkov, Adaptive reconnection-based arbitrary Lagrangian Eulerian method, *J. Comput. Phys.* 299 (2015) 902–939.
- [40] R. Loubère, P.-H. Maire, M. Shashkov, J. Breil, S. Galera, ReALE: A reconnection-based arbitrary-Lagrangian-Eulerian method, *J. Comput. Phys.* 229 (12) (2010) 4724–4761.
- [41] V. Dobrev, P. Knupp, T. Kolev, K. Mittal, R. Rieben, V. Tomov, Simulation-driven optimization of high-order meshes in ALE hydrodynamics, *Comput. & Fluids* 208 (2020) 104602.
- [42] P. Knupp, A method for hexahedral mesh shape optimization, *Internat. J. Numer. Methods Engrg.* 58 (2003) 319–332.
- [43] A. Menéndez-Díaz, C. González-Nicieza, A. Ernesto Álvarez-Vigil, Hexahedral mesh smoothing using a direct method, *Comput. Geosci.* 31 (4) (2005) 453–463.
- [44] G.A. Markou, Z.S. Mouroutis, D.C. Champsis, M. Papadrakakis, The ortho-semi-torsional (OST) spring analogy method for 3D mesh moving boundary problems, *Comput. Methods Appl. Mech. Engrg.* 196 (4–6) (2007) 747–765.
- [45] Y. Di, J. Yang, T. Sato, An operator-split ALE model for large deformation analysis of geomaterials, *Int. J. Numer. Anal. Methods Geomech.* 31 (12) (2007) 1375–1399.
- [46] D.A. Field, Laplacian smoothing and delaunay triangulations, *Commun. Appl. Numer. Methods* 4 (1988) 709–712.
- [47] D. Vartziotis, T. Athanasiadis, I. Goudas, J. Wipper, Mesh smoothing using the Geometric Element Transformation Method, *Comput. Methods Appl. Mech. Engrg.* 197 (45–48) (2008) 3760–3767.
- [48] D. Vartziotis, J. Wipper, B. Schwald, The geometric element transformation method for tetrahedral mesh smoothing, *Comput. Methods Appl. Mech. Engrg.* 199 (1) (2009) 169–182.
- [49] D. Vartziotis, J. Wipper, The geometric element transformation method for mixed mesh smoothing, *Eng. Comput.* 25 (2009) 287–301.
- [50] D. Vartziotis, J. Wipper, A dual element based geometric element transformation method for all-hexahedral mesh smoothing, *Comput. Methods Appl. Mech. Engrg.* 200 (9–12) (2011) 1186–1203.
- [51] S. Meduri, M. Cremonesi, U. Perego, An efficient runtime mesh smoothing technique for 3D explicit Lagrangian free-surface fluid flow simulations, *Internat. J. Numer. Methods Engrg.* 117 (4) (2019) 430–452.
- [52] D.A. Field, Laplacian smoothing and delaunay triangulations, *Commun. Appl. Numer. Methods* 4 (6) (1988) 709–712.
- [53] S.H. Lo, A new mesh generation scheme for arbitrary planar domains, *Internat. J. Numer. Methods Engrg.* 21 (8) (1985) 1403–1426.
- [54] Y. Guo, C. Wang, Z. Ma, X. Huang, K. Sun, R. Zhao, A new mesh smoothing method based on a neural network, *Comput. Mech.* 69 (2) (2022) 1–14.
- [55] H.-Y. Kim, H.-G. Kim, A hexahedral-dominant FE meshing technique using trimmed hexahedral elements preserving sharp edges and corners, *Eng. Comput.* 38 (5) (2022) 4307–4322.
- [56] J. Aymone, E. Bittencourt, G. Creus, Simulation of 3D metal-forming using an arbitrary Lagrangian-Eulerian finite element method, *J. Mater. Process. Technol.* 110 (2) (2001) 218–232.
- [57] A.-M. Zhang, S.-M. Li, P. Cui, S. Li, Y.-L. Liu, A unified theory for bubble dynamics, *Phys. Fluids* 35 (3) (2023) 033323.
- [58] X. Cao, F. Ming, A. Zhang, L. Tao, Multi-phase SPH modelling of air effect on the dynamic flooding of a damaged cabin, *Comput. & Fluids* 163 (2018) 7–19.

- [59] R. Ni, J. Li, X. Zhang, X. Zhou, X. Cui, An immersed boundary-material point method for shock-structure interaction and dynamic fracture, *J. Comput. Phys.* 470 (2022) 111558.
- [60] Y. Liu, H. Ye, H. Zhang, Y. Zheng, Coupling phase-field LB-MP method for multiphase fluid-deformable solid interaction problems involving large density and viscosity contrasts, *Int. J. Appl. Mech.* 15 (06) (2023) 2350050.
- [61] D. Xiao, P. Yang, F. Fang, J. Xiang, C. Pain, I. Navon, Non-intrusive reduced order modelling of fluid-structure interactions, *Comput. Methods Appl. Mech. Engrg.* 303 (2016) 35–54.
- [62] C. Chen, W.-K. Shi, Y.-M. Shen, J.-Q. Chen, A.-M. Zhang, A multi-resolution SPH-FEM method for fluid-structure interactions, *Comput. Methods Appl. Mech. Engrg.* 401 (2022) 115659.
- [63] B. Xue, S.-P. Wang, Y.-X. Peng, A.-M. Zhang, Numerical simulation of structural damage subjected to the near-field underwater explosion based on SPH and RKPM, *Ocean Eng.* 266 (2022) 112447.
- [64] M. Mostafaiyan, S. Wießner, G. Heinrich, Moving least-squares aided finite element method (MLS-FEM): A powerful means to predict pressure discontinuities of multi-phase flow fields and reduce spurious currents, *Comput. & Fluids* 211 (2020) 104669.
- [65] C.S. Peskin, Flow patterns around heart valves: A numerical method, *J. Comput. Phys.* 10 (2) (1972) 252–271.
- [66] Peskin, S. Charles, The immersed boundary method, *Acta Numer.* 11 (2002) 479–517.
- [67] L. Kan, X. Zhang, An immersed MMALE material point method for FSI problems with structure fracturing, *Comput. Methods Appl. Mech. Engrg.* 396 (2022) 115099.
- [68] M. Shashkov, Closure models for multimaterial cells in arbitrary Lagrangian-Eulerian hydrocodes, *Internat. J. Numer. Methods Fluids* 56 (2008) 1479–1504.
- [69] E.J. Caramana, D.E. Burton, M.J. Shashkov, P.P. Whalen, The construction of compatible hydrodynamics algorithms utilizing conservation of total energy, *J. Comput. Phys.* 146 (1) (1998) 227–262.
- [70] E.J. Caramana, C.L. Rousculp, D.E. Burton, A compatible, energy and symmetry preserving Lagrangian hydrodynamics algorithm in three-dimensional cartesian geometry, *J. Comput. Phys.* 157 (1) (2000) 89–119.
- [71] J.S. Peery, D.E. Carroll, Multi-Material ALE methods in unstructured grids, *Comput. Methods Appl. Mech. Engrg.* 187 (3/4) (2000) 591–619.
- [72] P.D. Zavattieri, E.A. Dari, G.C. Buscaglia, Optimization strategies in unstructured mesh generation, *Internat. J. Numer. Methods Engrg.* 39 (1996) 2055–2071.
- [73] H.M. Tsai, A.S.F. Wong, J. Cai, Y. Zhu, F. Liu, Unsteady flow calculations with a parallel multiblock moving mesh algorithm, *AIAA J.* 39 (6) (2001) 1021–1029.
- [74] X. Chen, X. Zhang, An improved 3D MoF method based on analytical partial derivatives, *J. Comput. Phys.* 326 (2016) 156–170.
- [75] S. Galera, J. Breil, P.-H. Maire, A 2D unstructured multi-material Cell-Centered Arbitrary Lagrangian-Eulerian (CCALE) scheme using MOF interface reconstruction, *Comput. & Fluids* 46 (1) (2011) 237–244.
- [76] H. Ahn, M. Shashkov, Multi-material interface reconstruction on generalized polyhedral meshes, *J. Comput. Phys.* 226 (2007) 2096–2132.
- [77] W. Boscheri, M. Dumbser, D.S. Balsara, High-order ADER-WENO ALE schemes on unstructured triangular meshes-application of several node solvers to hydrodynamics and magnetohydrodynamics, *Internat. J. Numer. Methods Fluids* 76 (10) (2014) 737–778.
- [78] F. Qing, X. Yu, Z. Jia, Z. Li, A cell-centered Lagrangian discontinuous Galerkin method using WENO and HWENO limiter for compressible Euler equations in two dimensions, *Comput. Appl. Math.* 40 (6) (2021) 212.
- [79] Y. Luo, Q. Xiao, G. Shi, L. Wen, D. Chen, G. Pan, A fluid-structure interaction solver for the study on a passively deformed fish fin with non-uniformly distributed stiffness, *J. Fluids Struct.* 92 (2020) 102778.
- [80] F. Paraz, C. Eloy, L. Schouveiler, Experimental study of the response of a flexible plate to a harmonic forcing in a flow, *C. R. Méc.* 342 (9) (2014) 532–538.
- [81] J. Baiges, R. Codina, The fixed-mesh ALE approach applied to solid mechanics and fluid-structure interaction problems, *Internat. J. Numer. Methods Engrg.* (81) (2010) 1529–1557.
- [82] T. Tang, Y. Gu, Q. Li, J. Hua, X. Sun, Expanding fracture of steel cylinder shell by detonation drivings, *Explos. Shock Waves* 23 (6) (2003) 529–533.
- [83] P. Yang, Y. Liu, X. Zhang, X. Zhou, Y. Zhao, Simulation of fragmentation with material point method based on guron model and random failure, *CMES* 85 (2012) 207–237.
- [84] H.S. Dong, High Energy Explosive and Some Related Properties, Science Press, Beijing, 1989.
- [85] G. Chen, Z. Chen, W. Xu, Y. Chen, X. Huang, Investigation on the J-C ductile fracture parameters of 45 steel, *Explos. Shock Waves* 27 (2) (2007) 131–135.
- [86] A.L. Gurson, Continuum theory of ductile rupture by void nucleation and growth: Part I - yield criteria and flow rules for porous ductile media, *J. Eng. Mater. Technol.* 99 (1) (1977) 297–300.
- [87] X. Lin, S.C. Fong, Ductile crack growth - II. Void nucleation and geometry effects on macroscopic fracture behavior, *J. Mech. Phys. Solids* 43 (12) (1995) 1953–1981.
- [88] S.C. Woodson, J.T. Baylot, Structural Collapse: Quarter-Scale Model Experiments, Technical Report SL-99-8, US Army ERDC, 1999.
- [89] B.A. Tegeler, C. Luo, A pragmatic design approach for internal blast scenarios, in: Structures Congress 2019: Blast, Impact Loading, and Research and Education, 2019.